Contributions to Mineralogy and Petrology (2024) 179:28
https://doi.org/10.1007/s00410-024-02097-1

ORIGINAL PAPER

Microstructural and isotopic analysis of shocked monazite from the Hiawatha impact structure: development of porosity and its utility in dating impact craters

William R. Hyde[1] · **Gavin G. Kenny**[2] · **Martin J. Whitehouse**[2] · **Richard Wirth**[3] · **Vladimir Roddatis**[3] · **Anja Schreiber**[3] · **Adam A. Garde**[4] · **Anders Plan**[5] · **Nicolaj K. Larsen**[1]

Received: 23 June 2023 / Accepted: 11 January 2024
© The Author(s) 2024

Abstract

U–Pb geochronology of shocked monazite can be used to date hypervelocity impact events. Impact-induced recrystallisation and formation of mechanical twins in monazite have been shown to result in radiogenic Pb loss and thus constrain impact ages. However, little is known about the effect of porosity on the U–Pb system in shocked monazite. Here we investigate monazite in two impact melt rocks from the Hiawatha impact structure, Greenland by means of nano- and micrometre-scale techniques. Microstructural characterisation by scanning electron and transmission electron microscopy imaging and electron backscatter diffraction reveals shock recrystallisation, microtwins and the development of widespread micrometre- to nanometre-scale porosity. For the first time in shocked monazite, nanophases identified as cubic Pb, Pb_3O_4, and cerussite ($PbCO_3$) were observed. We also find evidence for interaction with impact melt and fluids, with the formation of micrometre-scale melt-bearing channels, and the precipitation of the Pb-rich nanophases by dissolution–precipitation reactions involving pre-existing Pb-rich high-density clusters. To shed light on the response of monazite to shock metamorphism, high-spatial-resolution U–Pb dating by secondary ion mass spectrometry was completed. Recrystallised grains show the most advanced Pb loss, and together with porous grains yield concordia intercept ages within uncertainty of the previously established zircon U–Pb impact age attributed to the Hiawatha impact structure. Although porous grains alone yielded a less precise age, they are demonstrably useful in constraining impact ages. Observed relatively old apparent ages can be explained by significant retention of radiogenic lead in the form of widespread Pb nanophases. Lastly, we demonstrate that porous monazite is a valuable microtexture to search for when attempting to date poorly constrained impact structures, especially when shocked zircon or recrystallised monazite grains are not present.

Keywords Monazite · Hypervelocity impact · Shock metamorphism · SIMS U–Pb · Hiawatha · Radiogenic Pb

Introduction

Constraining ages of impact events on Earth is key for our understanding of its evolution and the role of impact cratering. A reliable approach for precise radiometric dating of hypervelocity impact structures is U–Pb age determination of shocked uranium-bearing accessory minerals found in impact-related material (French and Koeberl 2010; Jourdan et al. 2012). U-bearing minerals newly crystallised as primary phases in impact melt can provide the most precise impact ages (melt crystallisation ages; e.g., Davis 2008; Kenny et al. 2021). However, such occurrences are rare, and the majority of studies rely on inherited mineral grains. The extreme pressure–temperature conditions generated during shock metamorphism can result in the partial

---

Communicated by Othmar Müntener.

✉ William R. Hyde
william-hyde@outlook.com

[1] Globe Institute, University of Copenhagen, Øster Voldgade 5, 1350 Copenhagen K, Denmark

[2] Department of Geosciences, Swedish Museum of Natural History, SE-104 05 Stockholm, Sweden

[3] Helmholtz Centre Potsdam, GFZ German Research Centre for Geosciences, 14473 Potsdam, Germany

[4] Geological Survey of Denmark and Greenland, Øster Voldgade 10, 1350 Copenhagen K, Denmark

[5] Department of Geology, Lund University, Sölvegatan 12, 223 62 Lund, Sweden

Published online: 13 March 2024

to complete resetting of the U-Th-Pb system in U-bearing minerals (e.g., Krogh et al. 1984; Moser et al. 2011; Cavosie et al. 2015). Commonly used phases include zircon (e.g., Moser et al. 2011), monazite (e.g., Erickson et al. 2017b, 2020) and apatite (e.g., McGregor et al. 2018). More rarely, other accessory minerals are utilised, such as xenotime (Cavosie et al. 2021) and titanite (Papapavlou et al. 2018; McGregor et al. 2021). Zircon has been used as a geochronometer for radiometric dating of impact structures for decades (e.g., Krogh et al. 1984; Bohor et al. 1993), yielding many of the most precise impact ages in the current impact record of Earth (Schmieder and Kring 2020; Osinski et al. 2022). Consequently, microstructures in shocked zircon have been investigated in the greatest detail and constrained in terms of P–T-*t* (pressure–temperature-time) conditions in which they form, as well as their effect on Pb mobility (e.g., Cavosie et al. 2016; Erickson et al. 2017a; Timms et al. 2017; Plan et al. 2021). In comparison, U–Pb systematics and shock microtextures in monazite are relatively poorly understood in comparison.

Monazite, (La,Ce,Th)PO_4, grains exhibit a range of shock deformation microstructures in response to shock metamorphism and shocked monazite has been confirmed at several impact structures: e.g., Araguainha, Brazil (Tohver et al. 2012; Silva et al. 2016; Fougerouse et al. 2021), Vredefort, South Africa (Moser 1997; Hart et al. 1999; Flowers et al. 2003; Erickson et al. 2017b; Kovaleva and Dixon 2020; Fougerouse et al. 2021), Yarrabubba (Erickson et al. 2020) and Woodleigh (Fougerouse et al. 2021), Australia, and two Canadian impact structures, Carswell (Alwmark et al. 2017) and Haughton (Schärer and Deutsch 1990; Erickson et al. 2021). Microstructures in shocked monazite include mechanical twinning forming by a simple shear of the crystal lattice, intracrystalline plastic deformation (crystal-plastic) and recrystallisation textures (neoblastic) in response to more extreme impact conditions, all of which have been shown to variably perturb the U-Th-Pb systemics of monazite grains (Erickson et al. 2016). Advances in high-spatial resolution imaging techniques (e.g., electron backscatter diffraction [EBSD] analysis) and their integration with high-spatial resolution U–Pb age determination methods (e.g., secondary ion mass spectrometry, [SIMS]) has led to a better understanding of shock deformation and associated Pb loss in monazite and its use as reliable geochronometer for precise impact dating (Erickson et al. 2017b), in particular grains displaying polycrystallinity (Tohver et al. 2012; Erickson et al. 2017b, 2021) and microtwins (Moser et al. 2011; Erickson et al. 2017b; Fougerouse et al. 2020, 2021). Other recent discoveries in shocked monazite include nanoscale signatures of shock deformation (Seydoux-Guillaume et al. 2022) and a high-pressure shock-produced monazite polymorph with tetragonal symmetry (Erickson et al. 2019).

Little attention has been directed towards shocked monazite grains with numerous, sub-micrometre pores. We use the term ‘pores’ as it is non-specific to a formation process, following the reasoning of Martell et al. (2021). Here, we investigate monazite from two glaciofluvial (detrital) impact melt rock samples collected downstream from the Hiawatha impact structure, northwestern Greenland (Fig. 1A; Kjær et al. 2018; Hyde et al. 2023), and further explore the utility of monazite as an accurate and precise geochronometer for dating hypervelocity impact events. By integrating microstructural characterisation via EBSD and transmission electron microscopy (TEM) alongside state-of-the-art SIMS U–Pb geochronology, we highlight the previously unrecognised utility of porous shocked monazite. Additionally, nanoscale investigation of the grains offers further insights into the microstructural evolution of monazite in response to impact metamorphism, with a focus on the loss and/or retention of radiogenic Pb (Pb*). Through studying shocked monazite grains from samples that were previously dated using shocked zircon U–Pb geochronology (Kenny et al. 2022), we can directly compare and contrast how the two minerals, and particularly their U–Pb systems, respond to impact cratering. Zircon grains provided the first precise radiometric age of the crater (57.99 ± 0.54 Ma), as well as target rock ages that correlate with known lithologies in the immediate foreland of the structure (1915 ± 8 Ma), indicating a local origin of the samples (Fig. 1B; Kenny et al. 2022).

Methodology

Sample selection and description

Two pebble-sized, glaciofluvial impact melt rock samples, HW19-01 and HW19-05, were collected in 2018 from the glaciofluvial flood plain in front of the 31-km-wide, ice-covered Hiawatha impact structure (78.84° N 67.29° W), ~4 km downstream from the terminus of the main subglacial drainage channel originating from the protruding Hiawatha Glacier (Figs. 1A, 2; Kjær et al. 2018). Both HW19-01 and HW19-05 are clast-rich, hypocrystalline melt rocks and were selected for this study based on the previous confirmation of inherited monazite grains situated within the melt matrix (Figs. 2E, S1; Hyde et al. 2023). No monazite grains were observed within polycrystalline lithic clasts (e.g., orthogneiss) in either sample.

Analytical procedures and sample preparation

Samples HW19-01 and HW19-05 (Fig. 2) were disaggregated to fine sand using a jaw crusher and a puck-and-ring-style mill. Heavy minerals were concentrated by Franz magnetic and heavy liquid density separation (methylene

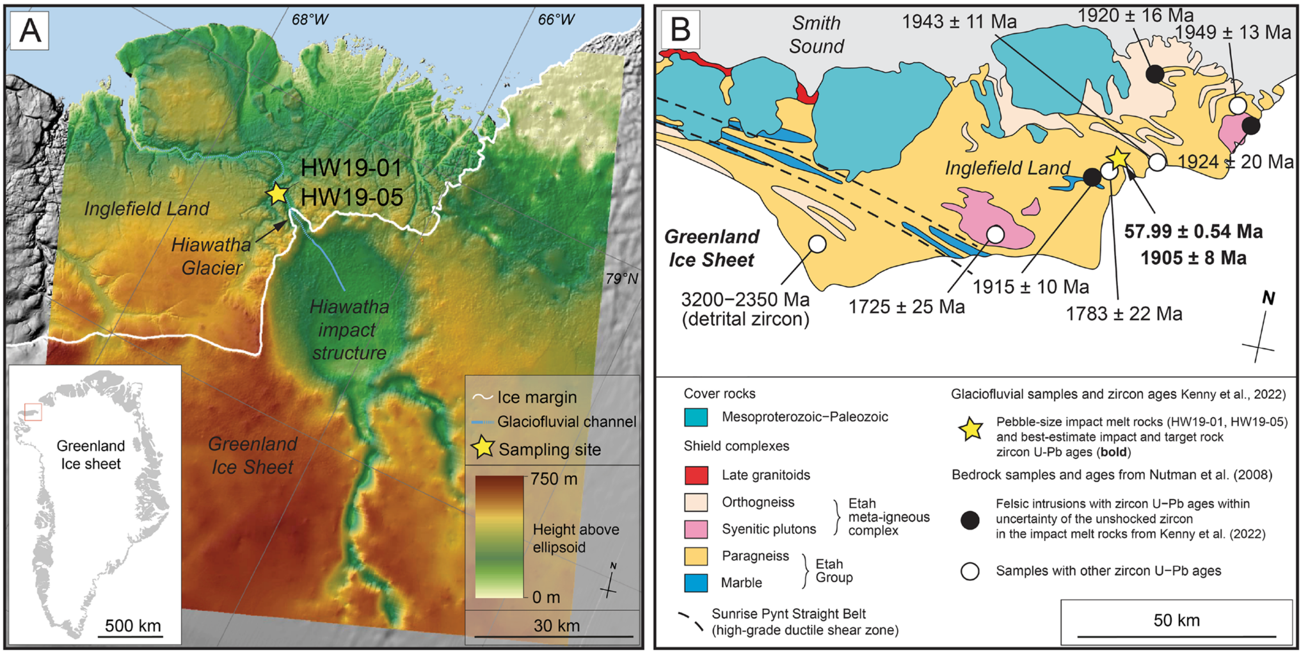
A
68°W
66°W
79°N
HW19-01
HW19-05
Inglefield Land
Hiawatha Glacier
Hiawatha impact structure
Greenland Ice Sheet
Greenland Ice sheet
500 km
Ice margin
Glaciofluvial channel
Sampling site
750 m
Height above ellipsoid
0 m
N
30 km
B
Smith Sound
1943 ± 11 Ma
1920 ± 16 Ma
1949 ± 13 Ma
1924 ± 20 Ma
Inglefield Land
Greenland Ice Sheet
57.99 ± 0.54 Ma
1905 ± 8 Ma
3200–2350 Ma (detrital zircon)
1725 ± 25 Ma
1915 ± 10 Ma
1783 ± 22 Ma
N
Cover rocks
Mesoproterozoic–Paleozoic
Shield complexes
Late granitoids
Orthogneiss
Syenitic plutons
Etah meta-igneous complex
Paragneiss
Marble
Etah Group
Sunrise Pynt Straight Belt (high-grade ductile shear zone)
Glaciofluvial samples and zircon ages Kenny et al., 2022)
Pebble-size impact melt rocks (HW19-01, HW19-05) and best-estimate impact and target rock zircon U–Pb ages (bold)
Bedrock samples and ages from Nutman et al. (2008)
Felsic intrusions with zircon U–Pb ages within uncertainty of the unshocked zircon in the impact melt rocks from Kenny et al. (2022)
Samples with other zircon U–Pb ages
50 km

Fig. 1 **A** Bedrock topography map of the Hiawatha impact structure modified after Kjær et al. (2018). Inset map shows the location in northwest Greenland. White line represents the current ice margin of the Greenland Ice Sheet. Sample locations of HW19-01 and HW19-05 are marked by a star icon. Blue line marks the main subglacial drainage channel (solid) and its continuation in the foreland (dotted line), indicating the likely transportation pathway of the samples. **B** Geological map of Inglefield Land, northwest Greenland. Previously published zircon U–Pb ages for bedrock samples from Nutman et al. (2008) and best-estimate impact and target rock crystallisation ages (lower and upper intercept) from Kenny et al. (2022) are shown. The dominant U–Pb target rock age in the same impact melt rock samples (1915 ± 8 Ma) is indistinguishable from the ages (zircon U–Pb) of proximal felsic igneous intrusions in the adjacent foreland. Map was modified after Kenny et al. (2022) and Nutman et al. (2008)

iodide ~ 3.3 g/cm^3). Grains were picked under a binocular microscope, selecting all observed monazite grains. A total of 30 grains were collected: 27 from HW19-01 and three from HW19-05. The selected monazite grains were mounted and cast in a 2.5 cm-diameter epoxy mount (lab name for mount: mt2130) and then polished using a Struers Rotopol at a frequency of 150 rpm and applying multiple grades of diamond suspensions (6 µm and 1 µm) to expose grain interiors. To prepare the grains for microstructural analysis (EBSD), the mounts were also polished with colloidal silica. The exposed interiors of all grains were imaged using backscattered electron (BSE) atomic contrast imaging on a FEI Quanta FEG 650 SEM at the Swedish Museum of Natural History, Stockholm, Sweden. Energy dispersive X-ray spectroscopy (EDS) element maps were completed on the same SEM, as were EBSD analyses on ten deformed grains of interest. After EBSD imaging, the epoxy mount was cleaned and gold-coated in preparation for U–Pb geochronology by SIMS.

Electron backscattered diffraction

EBSD analysis was performed using an Oxford Instruments Nordlys detector and an Oxford Instruments Symmetry S3 detector (the system was upgraded during the course of the project). Grains were indexed for monazite using match units based on crystallographic data from Ni et al. (1995). Analytical conditions and parameters utilised were a working distance of ~ 18 mm, accelerating voltage of 20 kV, stage tilt of 70°, electron backscatter pattern binning of 4 × 4, EBSP gain set to "High", background defined with a collection of 128 frames, Hough resolution set to 60, and band detection minimum/maximum of 6/8 following procedures detailed in Kenny et al. (2022). Maps were collected with step sizes between 0.09 and 0.2 µm. The collection of all data was done in Oxford Instruments Aztec software and processed in Oxford Instruments Channel 5 software v.5.12 (Nordlys detector) and Oxford Instruments Crystal software (Symmetry detector). All pole figures were plotted to include all shown points in IPF orientation maps and are the lower hemisphere. A wildspike correction was applied

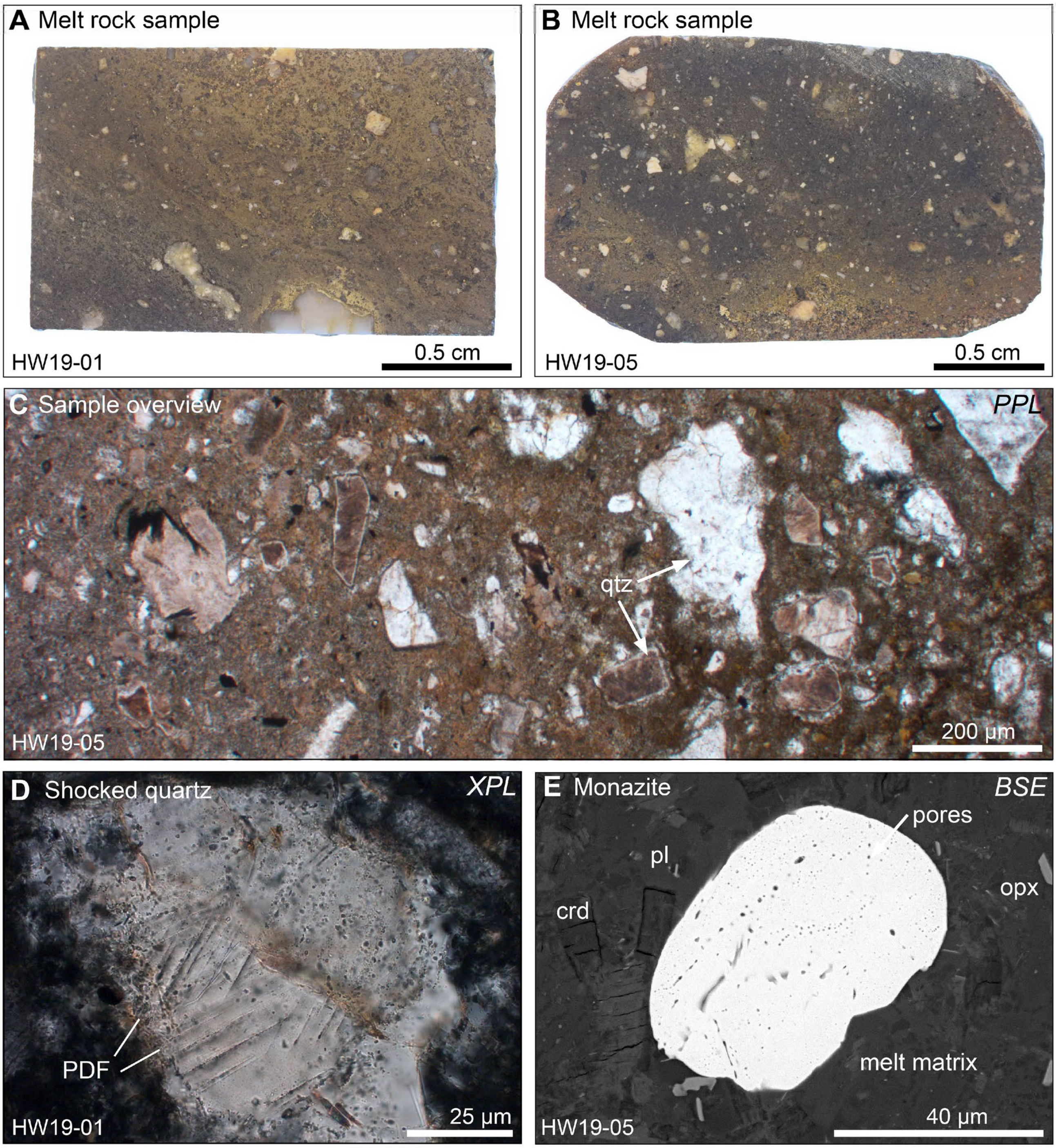
A Melt rock sample
HW19-01
0.5 cm
B Melt rock sample
HW19-05
0.5 cm
C Sample overview
PPL
qtz
HW19-05
200 µm
D Shocked quartz
XPL
PDF
HW19-01
25 µm
E Monazite
BSE
pores
pl
crd
opx
melt matrix
HW19-05
40 µm

Fig. 2 Imaging of detrital impact melt rock samples HW19-01 and HW19-05. **A, B** Cut surface of aphanitic, clast-rich impact melt rock samples. Images presented by Kenny et al. (2022). **C** Matrix and clasts within sample HW19-05, including abundant shocked quartz which is commonly toasted. **D** Shocked quartz clast with two or more sets of decorated planar deformation features (PDF). **E** Monazite grain displaying porosity situated within the melt matrix, which contains plagioclase (pl), orthopyroxene (opx) and pinnitised cordierite (crd) microlites. Note the arrangement of pores in a sublinear array. See Hyde et al. (2023) for more details on the nature of the samples. *PPL* plane polarised light, *XPL* cross polarised light, *BSE* backscattered electron

to all grains to remove isolated misindexed points and a nearest-neighbour zero solutions extrapolation based on between 1 and 3 nearest neighbours was also applied.

Transmission electron microscopy

Thirteen electron-transparent foils of monazite were prepared from eight monazite grains by focused ion beam (FIB) milling at the German research centre for Geosciences, Potsdam (GeoForschungsZentrum [GFZ]), using a Helios G4 UC FIB-SEM system. The TEM foils are 15–20 µm wide, 10–15 µm deep and ~ 100 nm thick and include a 1.5 µm thick protective Pt layer. For a detailed description of the sample preparation process see Wirth (2004, 2009). The TEM procedures applied follow those used in recent TEM investigations conducted at GFZ Potsdam, e.g., Kusiak et al. (2015, 2022) and Budzyń et al. (2021, 2022). TEM observations were performed using an FEI Tecnai™ G2 F20 X-Twin system at GFZ Potsdam, operated at 200 kV utilising a Schottky field emitter as an electron source and a post-column Gatan imaging filter (GIF Tridiem). The TEM is equipped with a Fishione high-angle annular dark field detector (HAADF) and EDAX X-Ray analyser enabling analytical and energy-filtered high-resolution transmission electron microscopy (ATEM, HRTEM). The HRTEM images were energy-filtered using a 10 eV window on the zero-loss peak. Scanning transmission mode (STEM) was used to measure X-ray intensities. Structural data such as d_{hkl} spacing and the angles between adjacent lattice planes of minerals were determined from selected area electron diffraction (SAED) patterns or diffraction patterns calculated by fast Fourier transform (FFT). The chemical composition of crystal matrix and nanoscale features was achieved using EDS analysis (STEM-mode) thus avoiding mass loss and acquisition times of ~ 60 s. Element maps and HR-STEM images were collected using a Thermo Fischer Scientific Themis Z electron microscope at GFZ Potsdam, operated at 300 kV and equipped with a CEOS corrector of spherical aberration installed at the probe-size, and a SuperX detector. The mapping was performed in the multi-frame mode with the probe current of about 50 pA to minimize possible radiation damages and to achieve good statistics.

Secondary ion mass spectrometry U–Pb

The monazite grains were analysed for U–Pb isotopic composition and date by SIMS in one analytical session on a CAMECA IMS1280 ion microprobe at the NordSIMS laboratory, Swedish Museum of Natural History. Analytical methods closely followed those described by Kirkland et al. (2009), with the exception that an Oregon Physics Hyperion H201 RF plasma high brightness oxygen source was used to produce O_2^- ions and the primary column tuned in critical focusing mode with a small (5 × 5 µm) raster applied to produce an analysis pit ~ 15 µm across. To increase the spatial resolution of the area that was effectively analysed in these complex monazite grains, the field of view on the sample was further restricted by closing the field aperture. This limited analysed ions to those from a central, approximately 6 µm by 6 µm square area (shown as a square inside the round to elliptical analysis pits in Figs. 3, 4 and 5). Standard monazite USGS 44069 was used as the primary reference standard, assuming a crystallization age of 424.9 Ma (Aleinikoff et al. 2006). The decay constant values of Steiger and Jäger (1997) were used. We applied a standard common Pb (Pbc) correction for all analysis, where Pbc was assumed to be largely introduced into crevices in the grains during the polishing stage of grain mount preparation and that Pbc is modern (i.e., 0 Ma in age) and has a modern-day Pb composition (Stacey and Kramers 1975). All U–Pb ages are calculated using the discordia (model-1) and isoplot online (Ludwig 1998; Vermeesch 2018). Only one data point in the entire dataset is excluded from the age calculations due to common Pbc overcorrection. All uncertainties in the text and figures are presented at the 2σ level unless otherwise stated, and the uncertainties in the data tables are presented at the 1σ level (Table S1).

Results

SEM and EBSD

All 30 monazite grains separated from HW19-01 and HW19-05 are < 150 µm in diameter (Fig. S2). In BSE images, grains display various microtextures and three morphological groups can be discerned: (i) mostly homogeneous grains with numerous sub-micrometre pores (Figs. 2E, 3), (ii) grains with similar porosity coexisting with partially filled, non-linear features (Fig. 4) and (iii) grains displaying polycrystallinity (Fig. 5).

Monazite grains containing abundant, densely packed pores is the most common grain texture (26 of 30 grains). Pores are generally submicrometre-scale and round. However, some grains contain larger micrometre-scale pores (Ø < 5 µm) which can be elongate (e.g., Fig. S2X). Pores appear both empty and variably filled (Figs. 3, S2). Pore arrangement varies between grains; some pores show alignment, being arranged in linear to sublinear arrays (Figs. 3A, S2), whereas many other grains contain pores that are apparently unaligned (Fig. 3B). Xenotime displaying similar porosity is also observed (Fig. S1). The monazite grains commonly exhibit greyscale zoning in BSE images, with rims or internal domains of contrasting atomic brightness. A correlation between zoning and the density and scale of pores is observed (grain 01-M03; Fig. 3B), where darker,

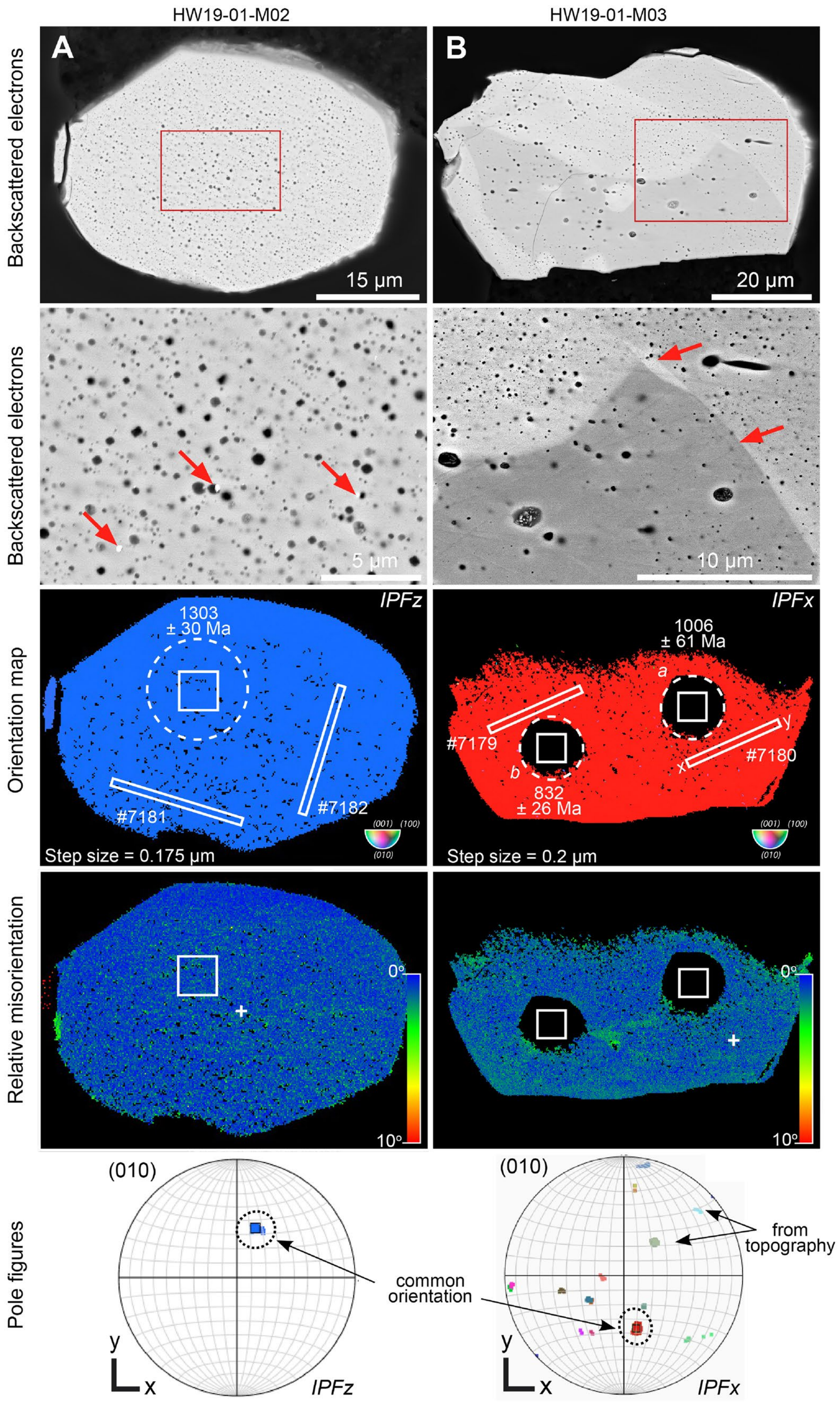
HW19-01-M02
HW19-01-M03
Backscattered electrons
A
B
15 µm
20 µm
Backscattered electrons
5 µm
10 µm
Orientation map
IPFz
IPFx
1303
± 30 Ma
1006
± 61 Ma
a
b
#7179
#7180
#7181
#7182
x
y
832
± 26 Ma
Step size = 0.175 µm
Step size = 0.2 µm
(001) (100)
(010)
Relative misorientation
0°
10°
Pole figures
(010)
common orientation
from topography
y
x
IPFz
IPFx

◂**Fig. 3** Microstructural characterisation of two porous monazite grains, HW19-01-M02 (**A**) and HW19-01-M03 (**B**). Backscattered electron (BSE) images show variable porosity. Red boxes show the locations of small-scale BSE image below. Note (arrows) sublinear arrays of nanoporosity and rare sub-micron bright inclusions within pores (**A**), and a relationship between greyscale zoning and porosity (**B**). Electron backscattered diffraction (EBSD) inverse pole figure (IPF) orientation maps show one common orientation across the exposed interior grain surface. SIMS spot locations for U–Pb analysis (dashed circle: U–Pb analysis pit (~ 15 µm across), solid squares: 6 µm × 6 µm area of sampled material), calculated $^{206}Pb/^{238}U$ apparent ages and locations of FIB cuts are shown (e.g., FIB #7181). FIB section #7180 is labelled with *x* and *y* for orientation (Fig. 6E). All uncertainties in the figures are presented at the 2σ level. Relative orientation maps are 10° degrees misorientation from an arbitrary point (cross). No crystal-plastic lattice strain is observed. The mottled effect seen is presumably due to porosity leading to areas of poor crystal indexing. Pole figures (010) show a single common orientation of the grains. Pole figures are coloured according to IPF orientation maps. Other recorded orientations (**B**) are from interaction with larger pores and are interpreted to be not true crystal orientations

relatively atomically light areas contain fewer, but larger pores, when compared to brighter pore-rich areas (Fig. 3B). Porous monazite grains generally show a single crystallographic orientation in IPF images and relative misorientation maps reveal little or no crystal-plastic lattice strain across the grains (Figs. 3, S3). No other microstructure indicative of structural deformation is observed (i.e., microtwins or recrystallised domains).

Two monazite grains, 01-M27 and 05-M02, contain non-linear, partially open features, referred to here as 'channels', as well as widespread porosity (Fig. 4), and are therefore also considered porous monazite. Internal channels vary in width and continuity, regularly terminating at grain exteriors, and do not resemble typical mechanical planar fractures (PF) or curvilinear fractures, nor do they uniformly follow cleavage. More grains with internal open areas are seen, although they show poor continuity and resemble isolated elongate pores or inclusions (Fig. S2). Small subdomains showing strong atomic contrast variation coincide with open channels and the same relationship between zoning and pore density described above is seen in these grains (Fig. 4). Crystal-plastic deformation (≤ 10° relative misorientation) is preserved across both monazite grains, including low angle (< 15°) subgrain boundaries that resemble polygonal misorientated domains (Fig. 4A). Changes in crystallographic orientation coincide with channels in grain 05-M02, with ~ 3–5° misorientation observed between separated domains (Fig. 4B). This grain also contains a single microtwin set with a twin-host disorientation relationship of 180°/ <100>, corresponding to a compositional (K_1) plane of (001) and a shear direction (η_1) of [100] following Erickson et al. (2016).

Polycrystalline textures are observed in two microstructurally complex monazite grains, 01-M23 and 05-M01 (Fig. 5). Kernel average misorientation maps reveal areas or subgrains with contrasting high and low levels of local misorientation, corresponding to high-strain (host) areas and low-strain (neoblasts) domains, respectively. Crystallographic orientation maps (all Euler) and IPF projections of both partially recrystallised grains display the orientation of all subdomains (Fig. 5). Grain 01-M23 contains isolated neoblasts within non-recrystallised areas, as well as a neoblastic area dominating the bottom of the grain, with large neoblasts up to ~ 18 µm across easily observed (Fig. 5B). Here, 120° triple junctions between impinging neoblasts are common. Neoblasts and host crystal domains are orientated ~ 90° from each other. Additionally, a microtwin set is observed oriented about 180°/ <101> (corresponding to a compositional (K_1) plane of ($\bar{1}01$) and a shear direction (η_1) of [101]; Erickson et al. 2016). This twin set exists within non-recrystallised areas and is cross-cut by neoblasts. Grain 05-M01 shows local misorientation more diffusively spread across the grain (Fig. 5A). Two groups of crystallographic orientations are again observed at ~ 90° relative misorientation. Both grains contain pores, although they are generally isolated and exhibit morphologies unlike those seen in the previously described porous grains (e.g., Figs. 3, 4). However, polygonal pore space situated between subdomains and neoblasts is abundant where the degree of impingement is low.

Chemical mapping

SEM–EDS chemical mapping of the monazite grains reveals that the observed greyscale zoning (Fig. 3B) corresponds to spatial variations in Th and rare earth elements ([REE]; Fig. 6). Brighter, relatively pore-rich areas are Th-rich and show an inverse relationship with Ce (REE). Most pores within the non-recrystallised monazite grains have compositions consistent with the host crystal, whereas larger pores contain notable concentrations (> 2 wt%) of various elements, e.g., Si, Fe, Al, K and Na (Fig. 6A). Similar concentrations of these elements are observed in non-linear channels, particularly when they terminate at the grain's exterior surface, and in larger polygonal pore spaces separating neoblasts (Fig. 6A–C).

Transmission electron microscopy

Thirteen FIB foils from six monazite grains were investigated using TEM/STEM techniques. Two grains were selected from each morphological group, corresponding to all grains presented above (Figs. 3, 4 and 5). The locations at which the FIB foils were cut are displayed there, and were chosen to cross-cut specific microstructures identified in the grains, for example, neoblasts, twins or Th/REE zonation.

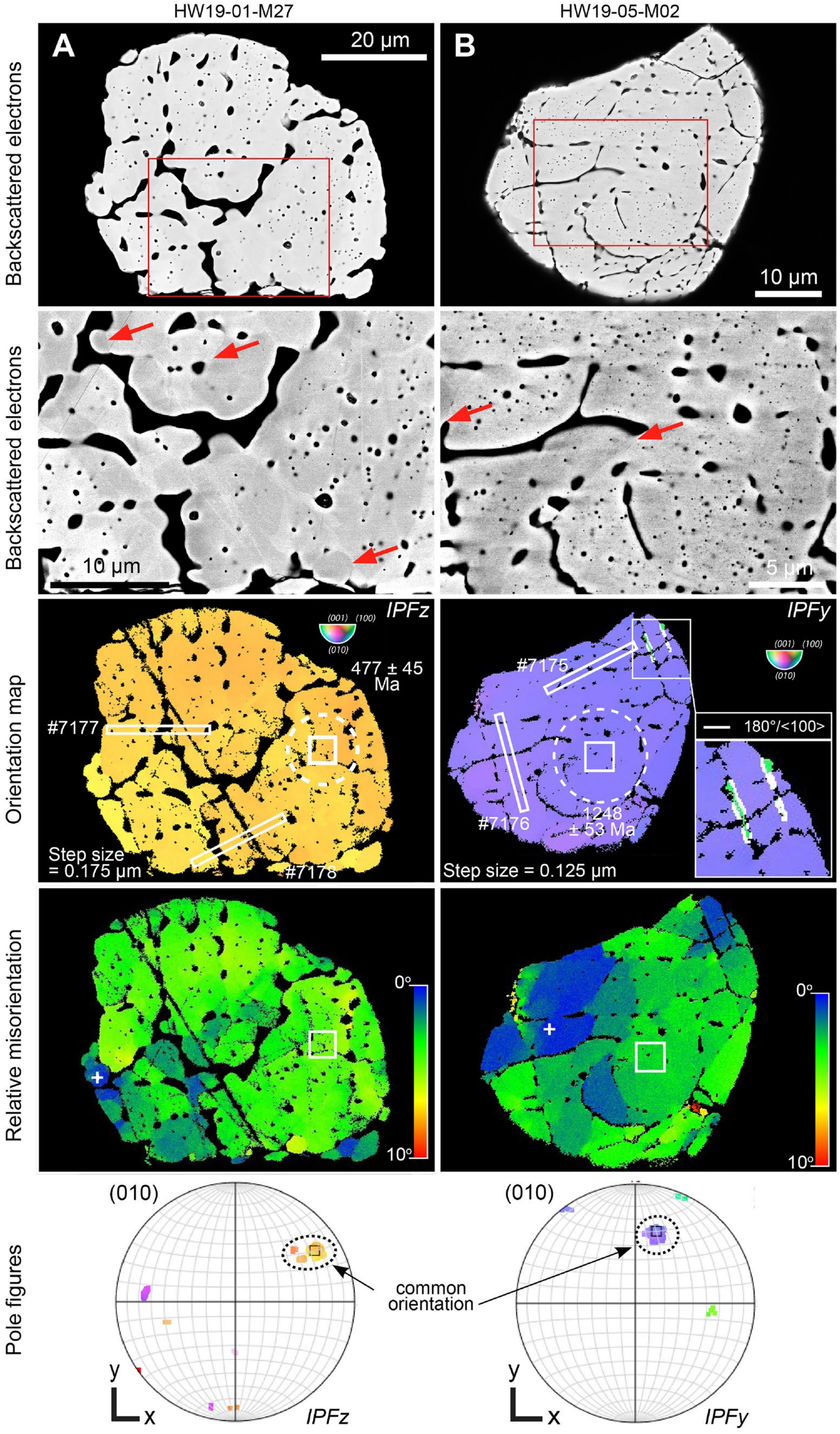
HW19-01-M27
HW19-05-M02
Backscattered electrons
Backscattered electrons
Orientation map
Relative misorientation
Pole figures
A
20 µm
B
10 µm
10 µm
5 µm
IPFz
(001) (100)
(010)
477 ± 45
Ma
#7177
#7178
Step size
= 0.175 µm
IPFy
#7175
#7176
1248
± 53 Ma
180°/<100>
Step size = 0.125 µm
0°
10°
0°
10°
(010)
(010)
common
orientation
y
x
IPFz
y
x
IPFy

◂**Fig. 4** Microstructural characterisation of two porous monazite grains with open channels, HW19-01-M27 (**A**) and HW19-05-M02 (**B**). BSE images of monazite grains showing micron-scale porosity and open, non-linear channels. Note (arrows) zoning and the formation of small, subdomains with variable BSE brightness (**A**), and a relationship between zoning and open channels (**B**). IPF orientation maps show one single orientation, apart from a 180°/<100> microtwin set (**B**; non-impact specific; Erickson et al. 2016). Crystal plastic lattice strain is observed across the grains exposed interior surface. Note small (2–5 µm) subdomains showing increased misorientation relative to the grain average orientation (**A**), and the interaction with channels and lattice strain (**B**). Pole figures (010) show a single common orientation of the grains. Linear unindexed feature is a scratch from grain polishing

Porous monazite

Grain 01-M02 (FIB foil #7181 and #7182) shows a high density of larger pores (Ø < 1 µm) that appear to be empty and randomly arranged (Fig. 7). Additionally, nanometre-scale pores (nanoporosity) are observed, which show alignment in linear arrays of increased concentration and contain bright inclusions (Fig. 7C). We find few defects in the crystal structure, observing only minor diffraction contrast variation preserved across the grain. Furthermore, the diffraction pattern FFT analysis (Fig. 7B) of HRTEM imaging of the crystal shows an undisturbed monazite diffraction pattern, indicating a single monazite crystal. FIB foil #7180 in grain 01-M03 cross-cuts a Th/REE zonation boundary observed from SEM-based observations (Figs. 3B, 6A; *x*–*y* coordinates) and exhibits a heterogenous distribution of nanostructures (Fig. 7E). A higher density of nanopores and lower dislocation density is observed in the relatively Th-rich region (Fig. 7F). Whereas in the relatively Th-poor region a greater abundance of non-linear dislocations are observed, which are pinned by, and link more abundant larger pores (Fig. 7G).

Curvilinear channels and non-spherical isolated inclusions within plastically deformed porous monazite grains are variably filled, either containing amorphous SiO_2 or a mixture of major elements (e.g., Si, Mg, Al, Fe; Fig. 8). The latter requires that it has been introduced from the surrounding matrix, likely in the form of impact-generated melt (Fig. 6B). These isolated inclusions and melt-filled channels are linked by large dislocations, visible in both HAADF (STEM) and BF (TEM) images (Fig. 8). Multiple, successive FIB cuts progressing through the grain and imaged consecutively show that the channels form a complex interconnected structure, extending throughout the monazite grain (Fig. S4). Both grains 01-M27 and 05-M02 show an increased density of nanoscale defects, relative to grains that show no crystal-plastic deformation (Figs. 3, 7). Dislocations are abundant and regularly form cell structures with low-angle grain boundaries, acting as barriers for dislocation motion, and together comprise extensive regions displaying blocky diffraction contrast (Fig. 8F). Steeply inclined curved dislocations with regular spacing are common, as well as nanoporosity (Fig. 8H).

Nanopores and Pb-rich nanophases

In addition to the larger submicrometre-scale pores that are observable in BSE images (e.g., Fig. 3), we find ubiquitous variably scaled nanopores in non-recrystallised grains (Figs. 7, 8). These structures range in size from ~ 20–300 nm, with two discernible groups: nanopores 100–300 nm in diameter and smaller features ~ 20–50 nm in diameter (Figs. 9A). TEM/STEM images reveal that bright, near-spherical inclusions (nanophases) are commonly situated within nanopores, located at the host crystal–pore boundary (Fig. 9). These nanophases are not seen within larger apparently empty pores (Fig. 7A). TEM-EDS scans and spot analyses show that these nanophases are consistently Pb-rich and that these phases are closely associated with variable amounts of amorphous Ca- and Si-rich material concentrated along larger nanopore walls (Fig. 9). Chemical comparison between the nanophases and surrounding pore space shows that no other external elements are present (Fig. S5D). Bright Pb-rich nanophases range in diameter from ~ 20–60 nm, depending on the scale of the pore they are situated in (Fig. 9C).

Diffraction patterns of individual Pb-rich nanophases located in 100-nm-scale nanopores were calculated by FFT from HRTEM images and SAED patterns. The diffraction patterns enable the measurement of observed d(hkl) spacings (Å), as well as of the angles between planes, which are compared with calculated values (Table 1). Diffraction patterns are randomly orientated, indicating that these features are individual crystallised phases, rather than Pb concentrations within the host monazite. Measured d(hkl) spacings from one nanophase (phase 1; Ø 25.8 nm; Fig. 9D) are 3.02, 2.56, 2.26 and 1.78 Å, which agree with d-spacings of Pb_3O_4 along the (220), $(\bar{2}\,12)$, (032) and (412) planes (3.115, 2.522, 2.189 and 1.791 Å, respectively; Gavarri and Weigel 1975) in the $[\bar{2}\,2\,\bar{3}]$ zone axis. This is confirmed by the agreement of observed and calculated angles between adjacent planes (Table 1). Measured d(hkl) spacings from another nanophase (phase 2; Ø 26.9 nm; Fig. 9F) are 3.80, 2.99 and 2.58 Å. These values align with d-spacings of Pb_2O_3 (3.871, 2.952 and 2.575 Å; Bouvaist and Weigel 1970), but also to a lesser extent cerussite ($PbCO_3$) along the $(\overline{11}\,1)$, $(1\,\bar{2}\,1)$ and $(0\,\bar{3}\,2)$ planes (3.587, 2.895 and 2.08 Å, respectively; Minch et al. 2010) in the [123] zone axis. However, when angles are calculated between adjacent planes, phase 2 shows good agreement with cerussite, consistently within 1.5–2° error of calculated values (Table 1), which is not true when calculated for Pb_2O_3. Furthermore, selected-area EDS analysis of phase 2 indexed as cerussite shows a clear increase in C,

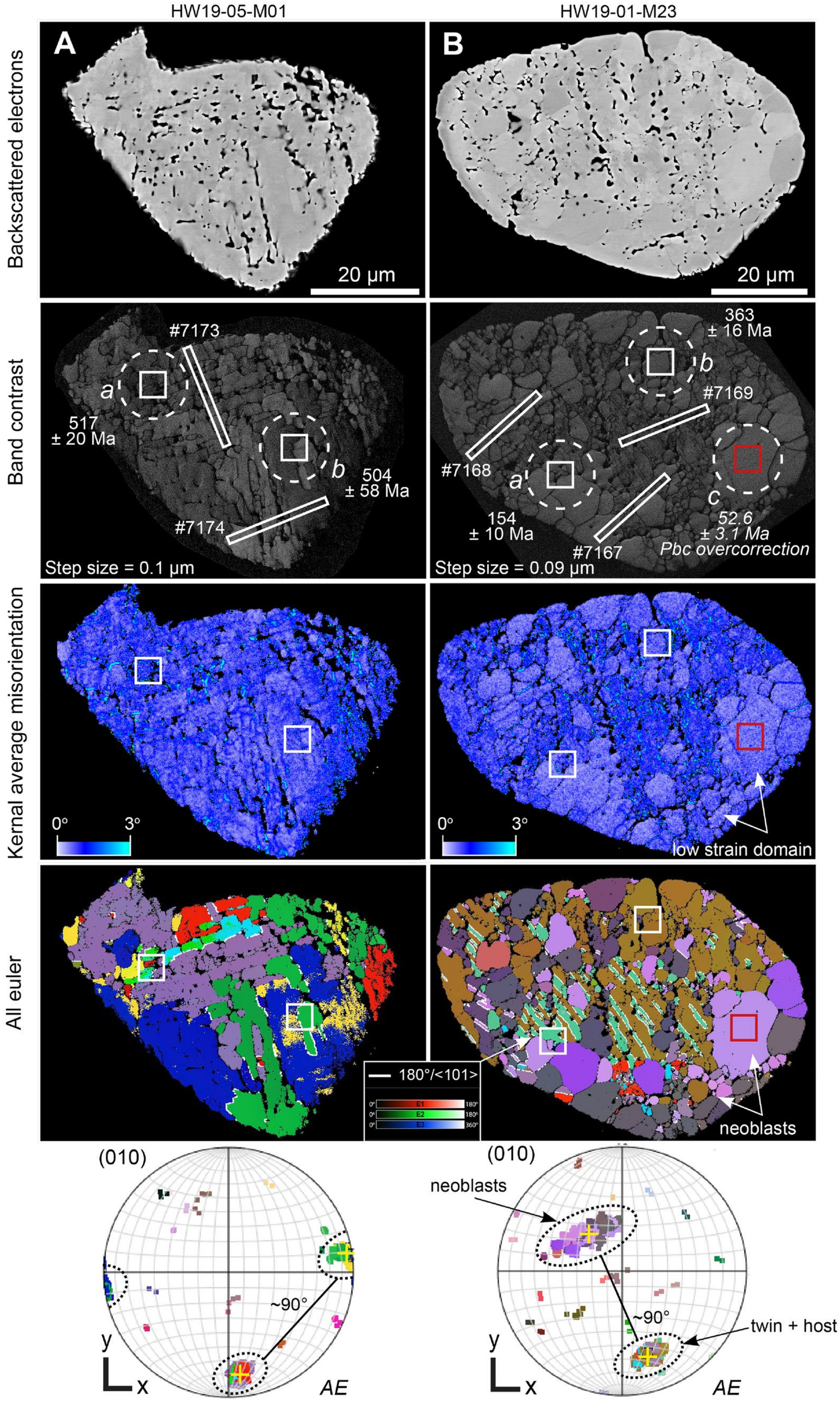
HW19-05-M01
HW19-01-M23
Backscattered electrons
Band contrast
Kernal average misorientation
All euler
A
B
20 µm
20 µm
#7173
a
517
± 20 Ma
b
504
± 58 Ma
#7174
Step size = 0.1 µm
363
± 16 Ma
b
#7169
#7168
a
c
154
± 10 Ma
52.6
± 3.1 Ma
Pbc overcorrection
#7167
Step size = 0.09 µm
0°
3°
0°
3°
low strain domain
180°/<101>
E1
E2
E3
neoblasts
(010)
~90°
y
x
AE
(010)
neoblasts
~90°
twin + host
y
x
AE

◂**Fig. 5** Microstructural characterisation of two partially recrystallised monazite grains, HW19-05-M01 (**A**) and HW19-01-M23 (**B**). BSE images show polycrystallinity. Open pores spaces are seen between neoblasts. Band contrast images of two grains containing SIMS spot locations for U–Pb analysis, calculated $^{206}Pb/^{238}U$ apparent ages and locations of FIB foil locations. Kernel average misorientation maps of recrystallised monazite grains show areas of low and high local misorientation, where neoblasts exhibit low strain domains (~0°). The orientation of subgrains is shown in orientation maps (All euler) and IPF images. Yellow cross (pole figures) represents the average orientation of the grouping. Grain 01-M23 (**B**) displays ~90° misorientation between two orientation groups in pole figures, one containing a shock microtwin set (10 $\overline{1}$) and host-crystal orientations, and the other neoblastic areas. The microtwin set revealed by white boarders is observed in two different orientations (green and purple; **B**). It is unclear what is recrystallised in grain 05-M01, however, a similar ~90° misorientation is observed between the two orientation groups

relative to the Pb_3O_4-indexed nanophase (Fig. 9), despite C having a low fluorescence yield. Analysis of four more nanophases reveals two indexed as Pb_3O_4 (phase 3 and 4), one as cerussite (phase 5), as well as the identification of a cubic Pb nanophase (phase 6) following the same procedure (Fig. S5E; Table S2).

Additionally, smaller near-spherical features which also show bright contrast reflecting high-density material are observed (Ø < 15 nm; Fig. 9E, G) and correspond to the widespread nanoscale features observed (Fig. 9A). EDS analysis of these features reveals a mixture of a monazite-like spectra with increases in Pb and Th, as well as Si and Ca, similar to the combined chemistry of larger nanopore-nanophase assemblages described above. Indexed FFT analysis of these nanoscale features reveals a monazite diffraction pattern (Fig. 9E). Furthermore, HR-STEM imaging reveals that lattice fringes are undisturbed (Fig. 9G) and, therefore, that there is no structural change from the host monazite.

Recrystallised monazite

TEM/STEM imaging of partially recrystallised grains shows that subgrains are common (Fig. 10). FIB foil #7167 (grain 01-M23) contains large homogenous regions of defect-free monazite with low diffraction contrast (orientation dependant; Fig. 10A, B). Additionally, small (Ø = 100–300 µm) subgrains containing dislocations, nanoporosity (including bright Pb-rich nanophases) and low-angle grain boundaries are situated within a central, sublinear domain (Fig. 10A, C). No nanopores or associated bright Pb-rich nanophases are observed within low-strain domains (neoblasts). Curvilinear, high-angle grain boundaries separate the two domains, with cell structures immediately adjacent to the darker, defect-free monazite (Fig. 10B). Areas of neoblasts with 120° triple junctions are observed in defect-free monazite (Fig. 10D).

FIB foil #7169 from the same grain shows similar microstructures. However, a microcrystalline domain contains aligned, elongate subgrains with strong diffraction contrast, each containing induvial cell structures and low-angle grain boundaries (Fig. 10E). Open, variably filled pore spaces separate these subgrains from the defect-free monazite with non-linear contacts (Fig. 10F, G). Isolated neoblasts are located within microcrystalline domains, frequently in association with external material occupying open pore space (Fig. 10H). FIB foil #7174 (grain 05-M01) contains similar elongate subgrains separated by open pore space filled with siliceous material, including individual microlites corresponding to silicate melt phases (Fig. 10J, K). Sharp, linear structures separate elongate subgrains and cut grain boundaries and cell structures (Fig. 10L).

SIMS U–Pb geochronology

A total of 39 U–Pb analyses were performed on 30 shocked monazite grains: thirty-five analyses on 27 grains separated from HW19-01 and four analyses on three grains separated from HW19-05 (Table S1). Considering both samples together, 34 analyses were obtained from grains with densely packed pores, including two analyses from grains with open, melt-bearing channels (Figs. 3, 4), and five analyses from two polycrystalline grains, targeted at either recrystallised or non-recrystallised domains, or a mixture of both textures (Fig. 5). The selection of analysis sites was based on prior BSE imaging of all grains and EBSD imaging of ten of the grains. No apparently undeformed grains were analysed, as none were found (Fig. S2). All grains show variable degrees of Pb loss, preserving a broad range of apparent ages, and no data points are concordant. It is worth mentioning here all Pb is radiogenic (Pb*), excluding measured Pbc. Calculated $^{206}Pb/^{238}U$ ages from both samples populate the same discordant distribution, defining a linear discordia trend between the Paleoproterozoic and the Late Paleocene (Fig. 11A).

Thirty-four analyses on monazite grains with pervasive porosity populate the centre of the field and preserve the oldest apparent ages, ranging from 477 ± 45 Ma up to 1549 ± 50 Ma (Fig. 11). Analyses from two grains displaying open melt-filled channels alongside porosity yield vastly different ages: grain 05-M02 records a relatively old apparent age of 1248 ± 53 Ma, while grain 01-M27 gives the youngest apparent age from all porous grains of 477 ± 44.6 Ma (Fig. 4). In two grains that show clear Th/REE zoning, analyses in Th-rich domains yield older apparent ages (Figs. 3, S2A), and retain higher Th/U ratios and Pb concentration (Fig. 6A; Table S1).

Analyses ($n = 4$) of two partially recrystallised grains reveal the youngest apparent ages and form the lower end of the discordant distribution, plotting closest to the lower intercept (Fig. 11B). One analysis (HW01-M23c) on the largest neoblast (~ 18 µm across) in the grain 01-M23 gave

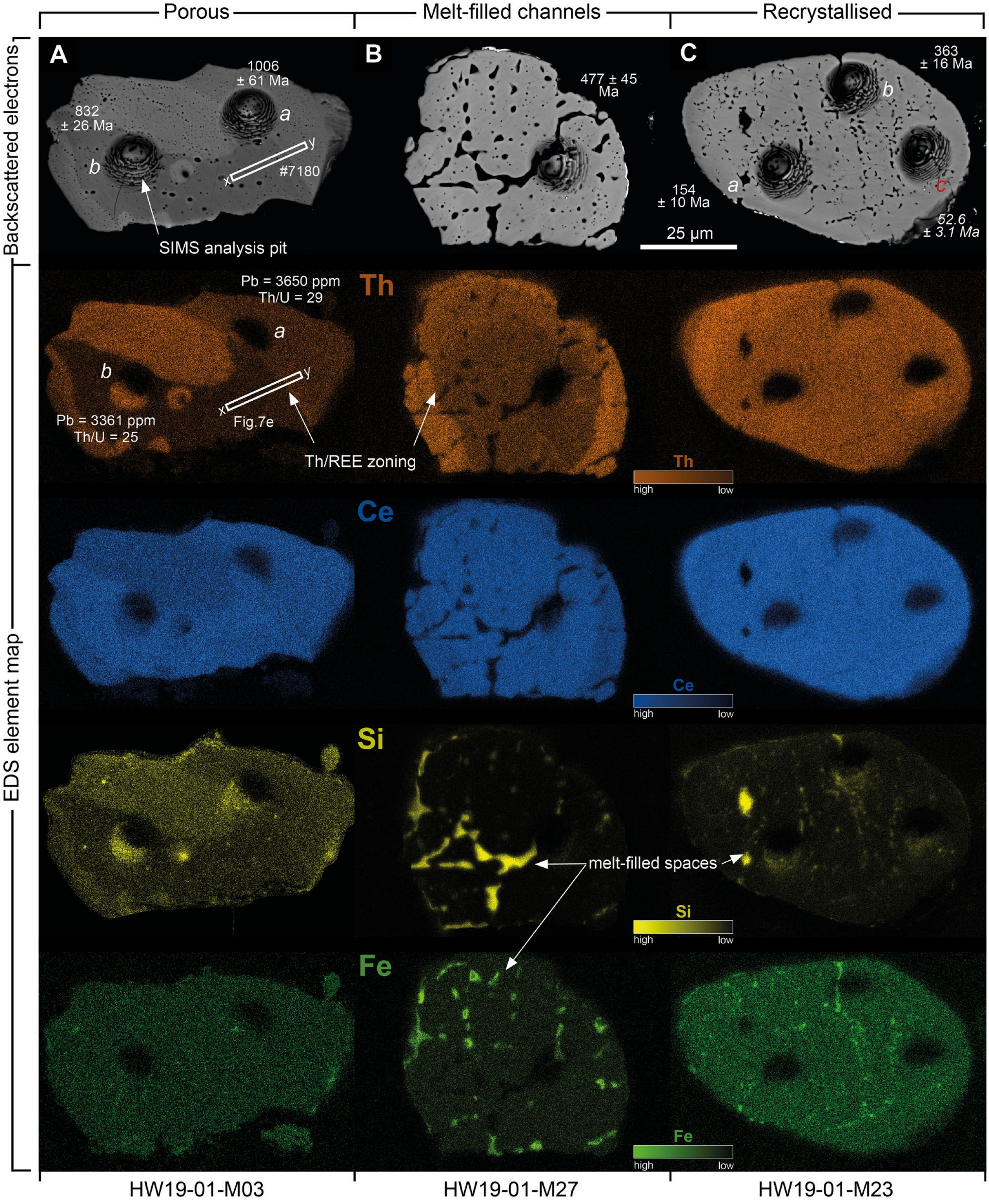
Porous
Melt-filled channels
Recrystallised
Backscattered electrons
EDS element map
A
1006
± 61 Ma
832
± 26 Ma
a
b
x
y
#7180
SIMS analysis pit
B
477 ± 45
Ma
C
363
± 16 Ma
b
154
± 10 Ma
a
c
52.6
± 3.1 Ma
25 µm
Pb = 3650 ppm
Th/U = 29
Th
a
b
Pb = 3361 ppm
Th/U = 25
x
y
Fig.7e
Th/REE zoning
Th
high
low
Ce
Ce
high
low
Si
melt-filled spaces
Si
high
low
Fe
Fe
high
low
HW19-01-M03
HW19-01-M27
HW19-01-M23

Fig. 6 SEM–EDS maps of monazite grains exhibiting various microtextures. **A** Porous grain (Fig. 3B), **B** porous grain with melt-filled channels (Fig. 4A) and **C** recrystallised grain (Fig. 5B). BSE images show SIMS analysis pits (~ 15 µm across), ^{206}Pb/^{238}U apparent ages and microstructures. Th and Ce (REE) EDS maps reveal chemical zoning and Si and Fe maps show siliceous melt injected into the grains or within open channels. Pb concentration (ppm) and Th/U ratios are higher in the Th-rich domain in grain HW19-01-M03 (**A**) from SIMS analysis (Table S1) and FIB section #7180 (*x*–*y*) cuts a Th-zonation boundary (Fig. 7E)

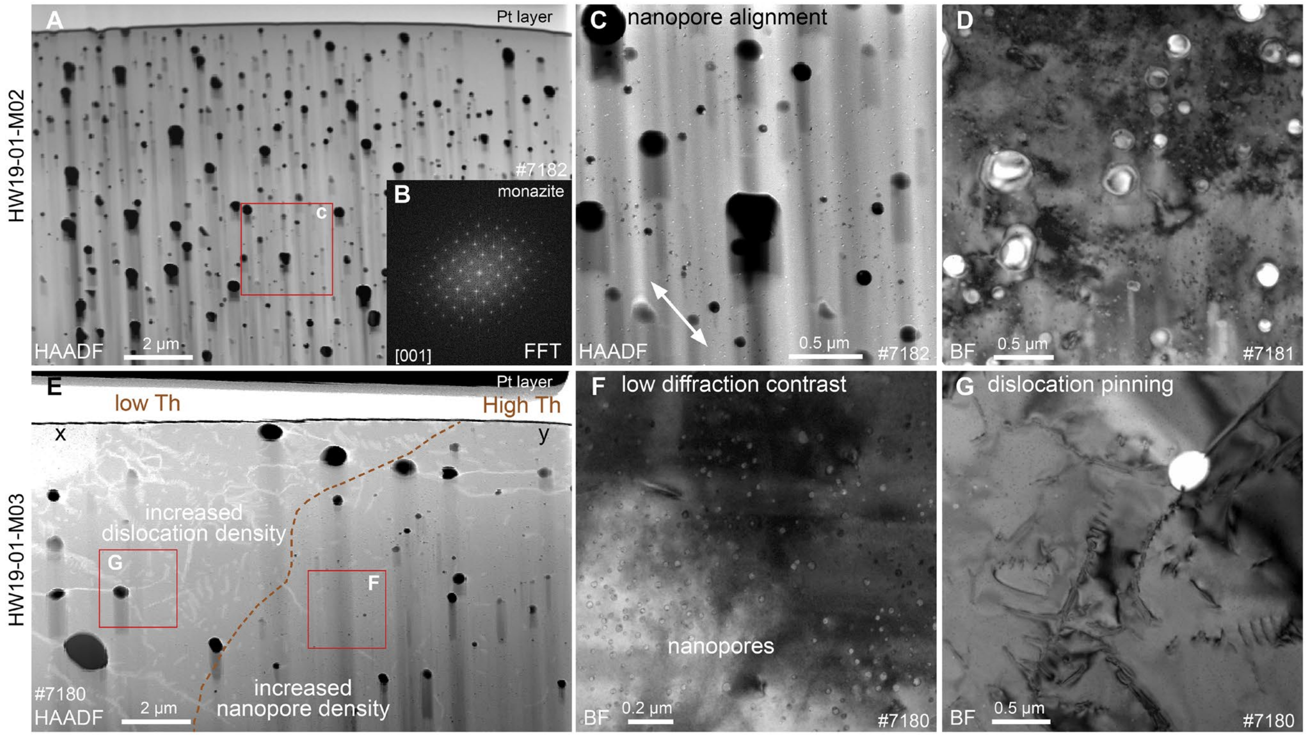

Fig. 7 TEM/STEM images of porous monazite showing variably scaled porosity. **A** Widespread sub-micrometre-scale pores apparently unaligned. Inset image (**B**) shows FFT of HRTEM analysis (not shown) of the monazite grain matrix, showing an undisturbed monazite diffraction pattern. **C** Arrangement of some nanopores into sublinear arrays (arrow) and bright nanoinclusions in pores. **D** Minor crystal defects in grain matrix and larger nanopores. **E** FIB section #7181 which cuts a Th zonation boundary (see *x–y,* Figs. 3, 6), showing heterogenous distribution of microstructures across the grain. Long dislocations link larger micrometre-scale pores on the left (Th-rich side), whereas lower dislocation density and an increased concentration of nanopores is observed on the right (Th-rich side). **F**) Ubiquitous nanoporosity in a defect-poor matrix. **G** Larger empty pore pinning a dislocation with low-angle grain boundaries. FIB foil and image type is shown in images and FIB foil locations within grains are given in Fig. 3. Red boxes show the location of small-scale images. *HAADF* High Angle Annular Dark Field (STEM mode), *BF* Bright Field (TEM mode). Black shadows in HAADF images are due to FIB cutting

the youngest ^{206}Pb/^{238}U apparent age of 52.6 ± 3.1 Ma (Fig. 5B); however, this analysis was not plotted in concordia space as the apparent ^{207}Pb/^{235}U ages could not be calculated, due to a slight overcorrection for Pbc (f_{206}% = 8.15) and is not used in the age calculations (Table S1). Analysis HW01-M23a targeted a mixed domain, containing recrystallised monazite and an area (~ 5 µm-wide) of a $(\bar{1}\,01)$ micro-twin, and preserved an older apparent age of 154 ± 10 Ma (Fig. 11D). The third analysis (HW01-M23b) was targeted at a predominately non-recrystallised domain, giving a yet older apparent age (363 ± 16 Ma). Two analyses from partially recrystallised grain 05-M01 both give apparent ages of ~ 500 Ma. The high f_{206}% recorded in all analyses of neoblastic grains is likely due to both the interstitial siliceous material located within pore spaces (Figs. 6C, 10), as well as the accumulation of detritus in these relatively topography-rich grains during polishing.

Apart from the one overcorrected age (HW01-M23c), no analyses have been filtered from the dataset (Table S1). When all monazite data are considered, the full discordant array yields a lower concordia intercept age of 56 ± 27 Ma (MSWD = 15) (Fig. 11B). Upon filtering the data based on grain microtextures, targeted analyses on neoblastic grains alone give a more precise lower concordia intercept age of 73 ± 15 Ma (MSWD = 0.76), whereas analyses on porous monazite grains alone give a less precise, lower intercept age of 46 ± 40 Ma (MSWD = 17) (Fig. 11C, D). The upper intercept for all data is 1911 ± 20 Ma, and upper intercepts for both the recrystallised (1937 ± 39 Ma) and porous monazite (1906 ± 25 Ma) data selections are within error of this age (Fig. 11).

Discussion

Combined SEM imaging, EBSD and TEM/STEM analyses, and SIMS age determination of shocked monazite from two detrital impact melt rocks collected near the Hiawatha impact structure, northwest Greenland, provides, among other insights, new constraints on how monazite responds

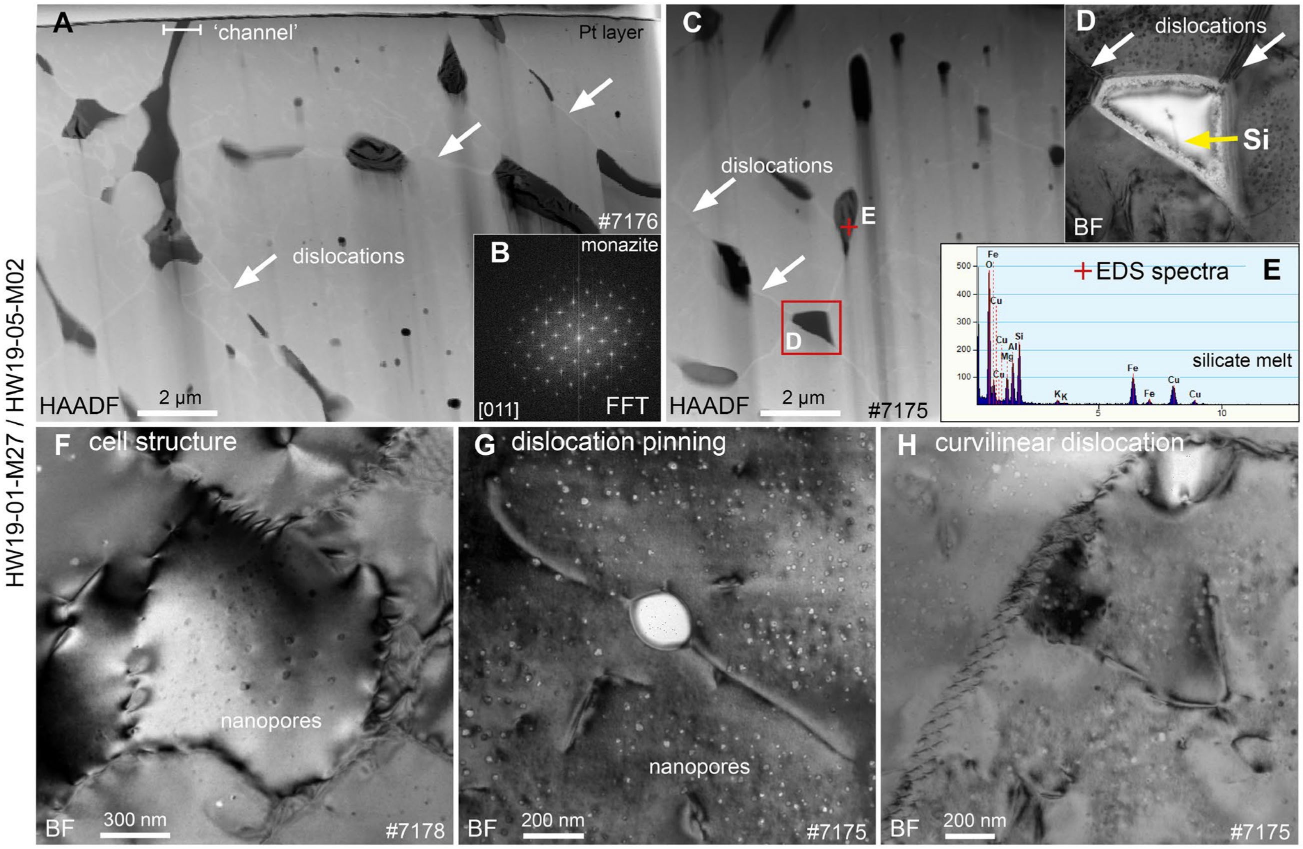
HW19-01-M27 / HW19-05-M02
A
'channel'
Pt layer
dislocations
#7176
HAADF
2 µm
B
monazite
[011]
FFT
C
dislocations
E
D
HAADF
2 µm
#7175
D
dislocations
Si
BF
EDS spectra
E
silicate melt
Fe
O
Cu
Cu
Si
Al
Mg
Cu
Fe
Fe
Cu
Cu
F cell structure
nanopores
BF
300 nm
#7178
G dislocation pinning
nanopores
BF
200 nm
#7175
H curvilinear dislocation
BF
200 nm
#7175

Fig. 8 TEM/STEM images of porous monazite with open melt-filled channels. Images **A** and **C** display long dislocations linking larger pore spaces (white arrows), which trend with curvilinear melt-filled channels. FFT analysis **B** reveals an undisturbed monazite diffraction pattern. **E**) EDS spectra (STEM mode) of a pore showing elevations in Si, Al, Mg and Fe, likely corresponding to a siliceous impact melt. Cu is from TEM grids and not present in the monazite. **D** Non-spherical pore space filled with amorphous SiO_2, with dislocations originating from pore corners (arrows). **F–H** Cell structures with low-angle grain boundaries, dislocations and dislocation pinning, and elongate, high-angle curvilinear dislocations. Nanoporosity is seen in all images. FIB foil and image type are shown in images and FIB foil locations within grains is given in Fig. 4. HAADF (STEM mode), BF (TEM mode). See Fig. S4 for a video of successive FIB cuts in grain HW19-05-M02 (**A**), revealing an interconnected structure of open melt-filled channels

to shock texturally and isotopically. Specifically, this work offers (i) new understanding of the formation of textures and microstructures previously documented in shocked monazite, i.e., nanoscale observations of recrystallised and microtwin domains in monazite, (ii) insights into how the previously understudied texture of porous monazite forms as well as its utility in dating impacts, and (iii) additional support for a Late Paleocene age for the Hiawatha impact structure, northwest Greenland.

Monazite microstructures

Recrystallisation

Recrystallisation textures and shock microtwins in monazite have been documented at other impact structures, as well as in tectonically deformed monazite (e.g., Tohver et al. 2012; Erickson et al. 2017b, 2021). It has been shown that neoblasts grow by grain boundary migration, resulting in largely strain-free subgrains and that recrystallisation occurs in high-strain domains in the pre-impact crystal structure (Erickson et al. 2015, 2016). Our observations of neoblasts at the nanoscale also show defect-free material, indicating new growth of monazite post-impact, as well as displaying the direction of neoblasts grain boundary migration into high-strain domains (Fig. 10B). Neoblasts are commonly spatially associated with pockets of melt (Figs. 6C, 10H) that were probably injected into the monazite during fracture formation, similar to injected ellipsoidal inclusions of shock-induced partial melt observed in shocked zircon (Moser et al. 2011). This indicates that recrystallisation can be controlled by both strain and exposure to melt (both external and injected), and therefore also the location of the grains within the thermally heterogenous clast-rich melt.

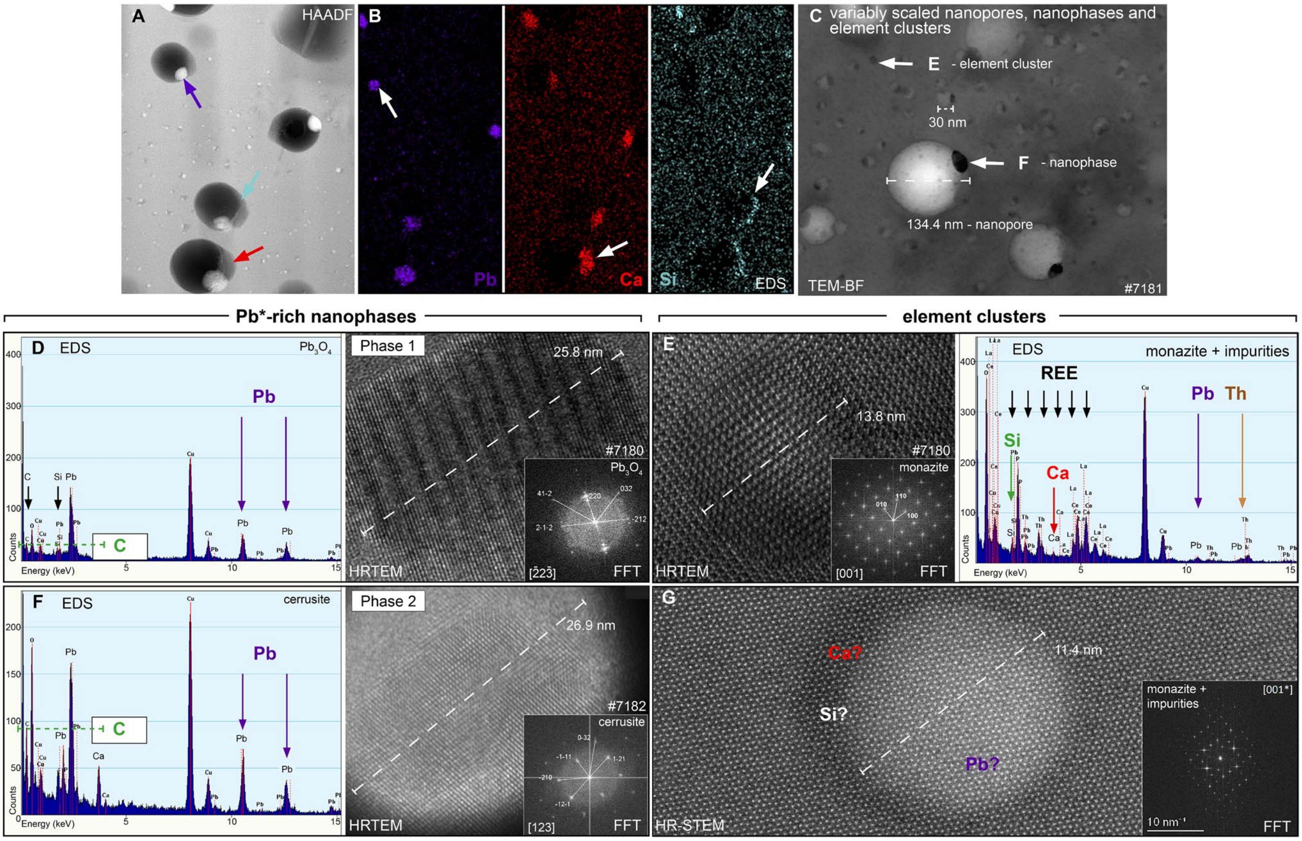
A
HAADF
B
Pb
Ca
Si
EDS
C variably scaled nanopores, nanophases and element clusters
E - element cluster
30 nm
F - nanophase
134.4 nm - nanopore
TEM-BF
#7181
Pb*-rich nanophases
element clusters
D EDS
Pb_3O_4
Pb
C
Counts
Energy (keV)
Phase 1
25.8 nm
#7180
Pb_3O_4
HRTEM
[223]
FFT
E
13.8 nm
#7180
monazite
HRTEM
[001]
FFT
EDS
monazite + impurities
REE
Si
Ca
Pb
Th
F EDS
cerrusite
Pb
C
Phase 2
26.9 nm
#7182
cerrusite
HRTEM
[123]
FFT
G
Ca?
Si?
Pb?
11.4 nm
monazite + impurities
[001*]
10 nm⁻¹
HR-STEM
FFT

Fig. 9 TEM/STEM/HR-STEM images of nanoscale features in porous monazite. **A** Multiple nanopores containing relatively large nanophases, as well as numerous smaller features with bright nanoinclusions (high-density clusters). **B** EDS scans of **A**. Pb is located within nanophases, whereas Ca- and Si-rich material is amorphous within pores situated next to Pb-rich nanophases. Coloured arrows in **A** show locations of element concentrations. **C** Pores showing variably scaled nanophases and element clusters (dark). **D**, **F** Phase identification of two Pb-rich nanophases through calculation of diffraction patterns from FFT of HRTEM images, revealing Pb_3O_4 and cerussite respectively. Note the large increase in carbon in nanophase indexed as cerussite (**F**), relative to nanophase indexed as Pb_3O_4 (**D**) from EDS spectra (STEM mode). **E**, **G** High-density element clusters (Ø < 15 nm). EDS analysis (STEM mode) reveals a monazite-like spectra (**E**), with significant Si, Ca, Pb and Th, however, FFT analysis shows that it retains a monazite diffraction pattern. HR-STEM image of element cluster (**G**) shows no structural difference between cluster and surrounding monazite crystal. Darker shadow-like contrast on the left is likely less dense material (Ca and Si) following Turuani et al. (2023; their Fig. 7). FFT analysis of cluster (**G**) gives a mixed diffraction pattern, indicating the combination monazite and impurities (e.g., Pb; brighter spots). FIB foil and image type is shown in images, and FIB foil locations within grains are given in Fig. 3. HAADF and EDS spectra (STEM mode), BF (TEM mode). HR-STEM: High-resolution STEM (Thermo Fischer Titan Themis). See Fig. S5 for more images of Pb-rich nanophases

Microtwins

Two different microtwin sets formed by simple shear of the crystal lattice are seen within the grains. The twin–host disorientation relationship of 180°/<100> displayed by a set of microtwins within a plastically deformed grain (Fig. 4B) has been produced in laboratory-based experiments (Hay and Marshall 2003; Seydoux-Guillaume et al. 2022) and observed in tectonically deformed monazite (Erickson et al. 2015), and is therefore not unique to hypervelocity impacts (Erickson et al. 2016). The twin-host disorientation relationship of 180°/<101>, observed here for a microtwin set within a partially recrystallised grain (Fig. 5B), has been reported as specific to hypervelocity impacting (Erickson et al. 2016). The pressure constraint has been estimated as 20 GPa, based on the discovery of well-constrained shock twins in zircon inclusions within shocked monazite grains containing a (10 $\overline{1}$) twin set (Erickson et al. 2016). Our TEM observations of the shock-specific (10 $\overline{1}$) microtwin set (FIB #7169) reveals aligned, elongate, defect-rich subgrains arranged in a narrow (~ 5 µm wide) domain that are bounded by sharp planar structures which truncate the subgrain defects (Fig. 10). These structures resemble planar deformation features in quartz and zircon (Goltrant et al. 1992; Leroux et al. 1999). The lack of defect-free material and 120° triple junctions inside the twin domain indicate that the twin did not undergo

Table 1 d-spacing in Ångström of two nanophases of this study compared to published values for Pb-oxides, Pb-sulphide, cubic Pb and cerussite and angles between adjacent planes for phase identification

d(hkl) observed		d(hkl) calculated								
HW19-01-M03	HW19-01-M02	Pb	PbS	PbO		PbO_2		Pb_2O_3	Pb_3O_4	$PbCO_3$
FIB #7180	FIB #7182	Cubic	Cubic	Orthrombic	Tetragonal	Orthrombic	Tetragonal	Monoclinic	Tetragonal	Orthrombic
Phase 1	Phase 2	Metal	Galena	Massicot	litharge	Scrutinyite	Platterite	Sesquioxide	Minium	Cerussite
Pb_3O_4	$PbCO_3$	$a=b=c=4.9505$	$a=b=c=5.9362$	$a=5.8931$	$a=b=3.9744$	$a=4.9858$	$a=b=4.9577$	$a=7.814$	$a=b=8.811$	$a=5.173$
				$b=5.4904$	$c=5.0220$	$b=5.6250$	$c=3.3879$	$b=5.627$	$c=6.5630$	$b=8.505$
				$c=4.7528$		$c=5.4626$		$c=8.465$		$c=6.111$
	3.80 (-1–11)			4.019		4.201	3.506	3.871		3.587 (-1–11)
3.02 (220)				3.069	3.117	3.26		3.028	3.115 (220)	
	2.99 (1–21)	2.858	2.97	2.947	2.81		2.797	2.952		2.895 (1–21)
	2.58 (0–32)		2.654	2.597		2.747		2.575		2.08 (0–32)
2.56 (-212)		2.475	2.423					2.507	2.522 (-212)	
2.26 (032)		2.214	2.098	2.279	2.123	2.177	2.217		2.189 (032)	
1.78 (412)		1.75	1.789	1.797	1.777	1.795	1.753		1.791 (412)	
Angles between adjacent planes		Bouad et al. (2003)	Zeuthen et al. (2020)	Garneir et al. (1990)	Boher et al. (1985)	Grocholski et al. (2014)	Bolzan et al. (1997)	Bouvaist and Weigel (1970)	Gavarri and Weigel (1975)[1]	Minch et al. (2010)[2]

Pb_3O_4 (Phase 1)			$PbCO_3$ (Phase 2)		
Planes	Calculated[1]	Observed	Planes	Calculated[2]	Observed
032|-212	43.47°	44°	0–32|121	34.8°	32.8°
032|220	58.2°	59.3°	0–32|-1–11	45°	44.3°
412|-212	34.26°	35.86°	-210|-1–11	57.37°	58°
412|220	44.06°	43°	-210|1–21	42.82°	43°

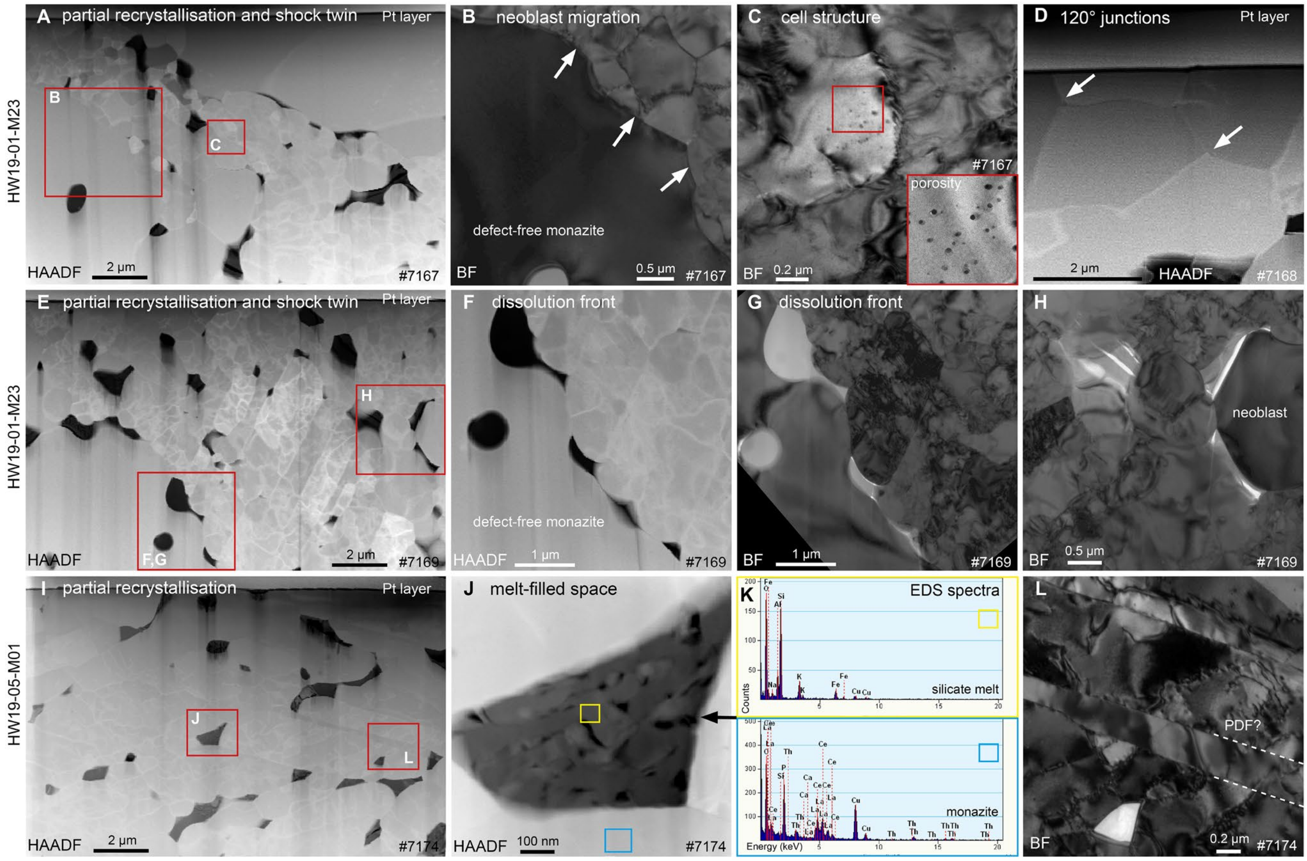
HW19-01-M23
A partial recrystallisation and shock twin
Pt layer
B
C
HAADF
2 µm
#7167
B neoblast migration
defect-free monazite
BF
0.5 µm
#7167
C cell structure
porosity
#7167
BF
0.2 µm
D 120° junctions
Pt layer
2 µm
HAADF
#7168
HW19-01-M23
E partial recrystallisation and shock twin
Pt layer
H
F,G
HAADF
2 µm
#7169
F dissolution front
defect-free monazite
HAADF
1 µm
#7169
G dissolution front
BF
1 µm
#7169
H
neoblast
BF
0.5 µm
#7169
HW19-05-M01
I partial recrystallisation
Pt layer
J
L
HAADF
2 µm
#7174
J melt-filled space
HAADF
100 nm
#7174
K
EDS spectra
silicate melt
monazite
Counts
Energy (keV)
L
PDF?
BF
0.2 µm
#7174

Fig. 10 TEM/STEM images of recrystallised monazite grains. **A** Central microcrystalline domain bounded by recrystallised domains. Image **B** shows defect-free monazite subgrain (neoblast) with curved subgrain boundaries indicating the direction of growth into the defect-rich microcrystalline domain (arrows). **C** Nanopores within poorly formed cell structure within a microcrystalline domain. **D** 120° triple junctions in neoblastic monazite. **E** Microtwin $(10\ \bar{1})$ domain (centre), containing elongate and aligned subgrains that contain a high density of crystal defects exhibit high degrees of diffraction contrast (orientation). **F**, **G** Contact between the defect-rich $(10\bar{1})$ microtwin and a large homogeneous subgrain, revealing a dissolution front preferentially exploiting elongate subgrain boundaries leading to curved edges. **H** Neoblasts surrounded by microcrystalline material, associated with proximal siliceous material. **I** Multiple, elongate subgrains with siliceous melt located in pore spaces (**J**), revealed from EDS analyses (**K**). **M** Linear features (PDF?) that separate elongate subgrains and truncate lattice-defects in image **I** Red boxes in images show locations of small-scale images. FIB foil and image type are shown in images and FIB foil locations within grains are given in Fig. 5. HAADF (STEM mode), BF (TEM mode)

instantaneous recrystallisation, which agrees with similar observations and conclusions from Fougerouse et al. (2020). The growth of discrete neoblasts proximal to interstitial siliceous melt in the twin domains (Fig. 10H) suggests melt injections led to later recrystallisation of high-strain areas, after twin formation.

Melt-bearing channels and crystal-plastic deformation

We also present new observations of melt-bearing channels and associated crystal-plastic deformation at the nanoscale. The melt-filled channels are linked with isolated melt-filled inclusions via large curvilinear dislocations (Figs. 4, 8). The resulting complex interconnected structure (Fig. S4), where the melt preferentially exploited curvilinear dislocations in the monazite crystal structure (Fig. 8A), are analogous to melt injections along curvilinear fractures previously described from shocked zircon (Moser et al. 2011). The accommodation of so much impact melt inside the monazite grains (Figs. 8, 6B) implies localised removal of the host, probably through in situ melting, or that the injection of melt into fractures led to fractures being forced open. In shocked zircon, the above mentioned melt film injections are locally associated with small, misorientated polygonal subdomains described as showing a ‘incipient granular texture’ (Moser et al. 2011, p 128). We observe similar subdomains in shocked monazite with elevated misorientation in close proximity to injected melt (Fig. 4D).

Lattice strain is recorded across the polished interior surfaces (Fig. 4) and expressed as an increased density of crystal defects at the nanoscale, including distinct nanoscale cell structures, low-angle subgrain boundaries and large

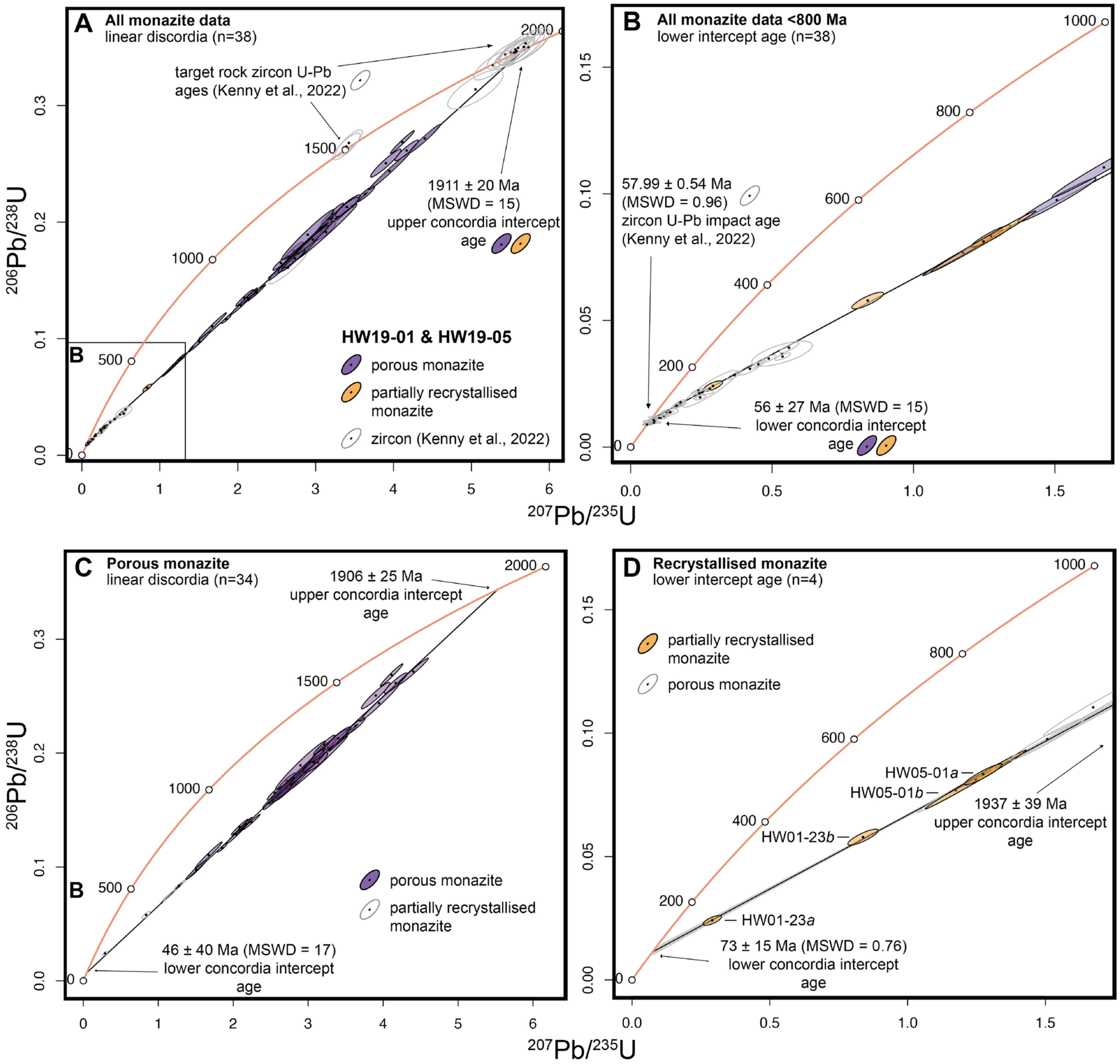

Fig. 11 Calculated monazite ^{206}Pb/^{238}U apparent ages from SIMS analyses projected on conventional concordia diagrams. **A, B** All SIMS U–Pb monazite data (n = 38) from samples HW19-01 and HW19-05. Data from porous (purple ellipses) and recrystallised (orange ellipses) grains yield a linear discordia. Calculated ^{206}Pb/^{238}U apparent ages < 800 Ma (**B**). Recrystallised monazite grain data show increased Pb loss relative to non-recrystallised grains. Upper and lower concordia intercept age of 1911 ± 20 Ma (MSWD = 15) (**A**) and 56 ± 27 Ma (**B**), respectively, are within analytical error of zircon U–Pb target rock and best estimate impact ages (white ellipses) from the same samples from Kenny et al. (2022). **C** Discordant array from porous grain data only (*n* = 34). Upper and lower concordia intercept age of 1906 ± 25 Ma and 46 ± 40 Ma (MSWD = 17) are both within analytical error of monazite and zircon U–Pb intercept ages (**A** and **B**). **D** Analysis-labelled data from recrystallised grains only (n = 4). No analysis displays complete Pb loss, due to analyses incorporating variably reset material (Fig. 5) and the retention of Pb* in Pb-rich nanophases (Figs. 9, 10). Upper and lower concordia intercept age of 1937 ± 39 Ma and 73 ± 15 Ma (MSWD = 0.76) are both within analytical error of monazite and zircon U–Pb intercept ages (**A** and **B**). One data point (HW01-M23c) is excluded due to a Pbc overcorrection (Fig. 5B). For probability (of concordance and equivalence) see all Data in Table S1

curvilinear dislocations (Fig. 8). Nanoscale features indicating crystal-plastic deformation are common in other shock-deformed minerals, including apatite, where dislocations and subgrains are also observed in response to shock (Cox et al. 2020). Similarities in mineral chemistry and structure between monazite and apatite is likely reflected in similar shock microstructures.

Sub- to micrometre-scale porosity

Pores ranging in scale from ~ 1 µm to 20 nm are observed within all monazite grains studied here. Larger pores (Ø > 500 nm) visible in BSE imaging are frequently arranged in sublinear to linear arrays (Figs. 3, S2). Monazite grains displaying porosity aligned in arrays have been reported from other impact structures (e.g., Flowers et al. 2003; Alwmark et al. 2017; Erickson et al. 2021), but rarely have pores observed as densely packed as those presented here (e.g., Fig. 3A). In the above-mentioned cases, pores are spatially associated with pre-existing structures (e.g., host fractures (PFs) or twin boundaries) and likely formed during post-shock decompression. We present grains that have apparently similar arrays of pores but lack any such structures and exhibit no clear crystallographic evidence of former planar structures (Fig. 3). We suggest that this is due to the annealing of host structures (e.g., PFs) during the post-impact high-temperature excursion when impact melt and the grains were interacting. Similar arrays of pores are observed in shocked apatite from various impact structures, although termed micro-vesiculation (McGregor et al. 2019, 2020), and a similar thermally dependant annealing mechanism has been proposed for shock-related relict pore arrays in apatite (McGregor et al. 2021). Long dislocations in the monazite grains that link larger sub-micrometre pores (Fig. 7E), and linear nanopore arrays (Fig. 7C), might represent partially annealed shock-induced fractures.

In contrast, the unaligned larger pores in many other monazite grains cannot have been controlled by preexisting planar or non-planar fractures. Erickson et al. (2021) presented vesiculated monazite grains with pores in an apparent random arrangement from the Haughton impact structure, Canada. However, unlike grains here, these monazite grains contain other features associated with shock metamorphism (e.g., microtwins, neoblasts) or deformation (e.g., low-angle grain boundaries). The striking observation of Th/REE zoning correlating with pore density (Figs. 3, 7E) can shed light on pore formation. Monazite grains with high degrees of porosity have been described elsewhere in non-impact samples, where a relationship between zonation and pore density is also seen (Turuani et al. 2022, 2023). In zircon, locally increased pore density is controlled by the weakening of the crystal structure in metamict zones (Geisler et al. 2007; Hay and Dempster 2009). However, the monazite grains studied here are not metamict (Fig. 7B), as self-healing of radiation damage occurs to a higher degree in monazite relative to zircon (Seydoux-Guillaume et al. 2004, 2018b). Nevertheless, lattice defects at the nanoscale influenced by charge imbalances or radiation damage associated with high Th/REE (Seydoux-Guillaume et al. 2018a) are present. During heating or post-shock decompression, these lattice defects possibly influenced pore formation. This algins with interpretations of pores in monazite, visible from BSE imaging, forming through vesiculation (Erickson et al. 2021), as well as similar mechanisms in other minerals, i.e., zircon (Wittmann et al. 2006; Zhang et al. 2011) and apatite (Barralet et al. 2002; Wittmann et al. 2013).

In summary, regarding the larger pores, we suggest that linear arrays of pores in monazite grains in our samples formed in association with now annealed structures such as fractures, whereas non-aligned pores formed preferentially in areas of increased crystal lattice instability, in response to post-shock decompression and/or heating. It is worth mentioning that our observations are specific to monazite grains from clast-rich impact melt rocks (Fig. 2); shocked monazite in impactites containing little or no melt will certainly behave differently.

Nanometre-scale porosity and Pb-rich nanophases

Additionally, a high density of nanometre-scale pores was found in non-recrystallised parts of monazite grains (Figs. 7, 8, 9 and 10). For the first time we also present spectacular radiogenic Pb-rich nanophases in shock-metamorphosed monazite (Fig. 9). Several different pure Pb- or Pb-rich phases, namely cubic Pb, Pb_3O_4 and cerussite, were identified from FTT analysis of HRTEM images and supported by EDS spectra (Figs. 9, S5D; Table 1). Previous work using TEM and/or atom probe tomography (APT) has documented Pb-rich nanophases in monazite grains from ultra-high-temperature (UHT) metamorphic rocks (Seydoux-Guillaume et al. 2003, 2018a, 2019; Turuani et al. 2022). Additionally, recent work has identified Pb_2O_3 and PbS as crystallising phases, as well as demonstrating an association with Si and Ca inside nanopores in monazite (Turuani et al. 2023). From high-resolution FIB-TEM/STEM diffraction patterns we further demonstrate that the near-spherical, bright Pb-rich nanophases in monazite are individual crystals (Figs. 9, S5), and that amorphous Ca- and Si-rich material is situated in the pores and not in a crystalised phase, as observed by Turuani et al. (2023). Additionally, we observe ubiquitous nanofeatures (Ø < 10 nm) of high-density material with monazite diffraction patterns and increases in anomalous element concentrations (e.g., Pb) mixed with monazite-like spectra from EDS analysis (Fig. 9E–G). These features are therefore not individual crystalline Pb-rich phases from undisturbed lattice fringes, but anomalous element concentrations within the monazite structure itself, termed here and elsewhere as 'clusters' (e.g., Turuani et al. 2023). Brighter intensity spots in the corresponding FFT analysis correspond to STEM scattering (impurities in the monazite crystal, e.g., Pb; Fig. 9G).

Establishing whether nanometre-scale porosity and associated Pb-rich nanophases in shocked monazite from the Hiawatha impact structure formed in response to the impact or may be, for example, pre-impact features of the grains, is critical to understanding their effects on impact-specific U–Pb systematics. In Antarctic UHT samples, Pb-rich nanophases in monazite are interpreted to from as a result of initial radiation damage-facilitated element mobility and accommodation of elements locally into element clusters over extended time periods (e.g., Fig. 9G). Subsequent precipitation of nanophases (e.g., Fig. 9D) occurs during interaction with fluids through dissolution–precipitation reactions during later retrograde metamorphism (Turuani et al. 2023; their Fig. 12). The first of the two stages proposed for Pb-rich nanophase formation (i.e. clustering of Pb* ± Ca ± Si through Th and U decay and resulting radiation damage; Turuani et al. 2023) must have occurred prior to the impact event. Significant Th and U decay requires extended geological time (billions of years), i.e. in monazite in Inglefield Land, northwest Greenland, between monazite crystallization at ~ 1.9 Ga, and the impact event at ~ 58 Ma (U–Pb zircon impact age; Kenny et al. 2022). The observation that neoblasts in shocked monazite lack Pb-rich nanophases and element clusters (Fig. 10) supports this, as recrystallisation would be expected to have expelled element clusters which are suggested to be pre-requisite to form Pb-rich nanophases via dissolution and precipitation (Turuani et al. 2023).

In this scenario, the question becomes whether the subsequent precipitation of Pb-rich nanophases in monazite also occurred pre-impact, or whether it may have occurred in response to the impact event. We see evidence here for greater interaction with siliceous melt, and associated fluids, than would be expected for monazite in an endogenic metamorphic setting (e.g., melt film injections; Figs. 6, 10). This interaction was sustained long enough for dissolution–precipitation reactions to occur, as cooling of an impact structure to ambient conditions can take up to hundreds of thousands of years, or even million-year timescales in the largest terrestrial craters (Abramov and Kring 2007; Schmieder and Jourdan 2013; Kenny et al. 2019). Furthermore, accounting for element cluster formation (1–2 Gyr), there is no record of another relatively recent high-temperature metamorphic event in Inglefield Land (Nutman et al. 2008) that could be assigned to the subsequent initiation of Pb-rich nanophase. Therefore, here we propose the hypervelocity impact event as the external high-T process.

The present study also expands the variety of crystalline Pb-rich phases observed in porous monazite (Figs. 9, S5D). The formation of cerussite nanocrystals (Ø ~ 25 nm; Fig. 9F; Table 1) demands the availability of carbon (either as C, CO and/or CO_2). Previous work has shown that carbonate-rich lithologies were present within the target sequence at the Hiawatha impact structure, and that macro-scale organic fragments are commonly located within the impact melt (Garde et al. 2022; Hyde et al. 2023). Furthermore, C has been demonstrated to be preserved in impact melt from other structures, for example, the Gardnos impact structure, Norway (Lindgren et al. 2019). This suggests that C was readily available and supports an impact-induced origin for the Pb-rich nanophases, as the immediate availability of appropriate elements is suggested to dictate the mineralogy of Pb-bearing nanophases in monazite (Turuani et al. 2023).

More work is required, however, to determine both the exact timing nanophase precipitation, for example during impact-related heating and/or impact melt-facilitated fluid-ingress into the monazite crystals, or possibly during prolonged cooling and hydrothermal alteration of the impact structure, as well as the controls on Pb-rich nanophase formation. Physico-chemical parameters controlling the initial state of the monazites lattice (i.e., Th/REE zoning, stress) have been shown to influence the accumulation of elements in monazite (Seydoux-Guillaume et al. 2002; Grand'Homme et al. 2016, 2018). The observation that we see higher concentrations of variably scaled porosity and Pb* nanophases, as well as Pb concentrations from SIMS analysis, in Th-rich domains of zoned grains supports this (Figs. 6, 7F). This suggests both that element clusters form from charge imbalance-induced element mobility (Th decay), and that the Th zonation indirectly has led to higher retention of Pb* by facilitating increased Pb-rich nanophase precipitation. Additionally, temperature (i.e., the location of the grains within the heterogenous impact melt; Fig. 2E) was presumably a major control on dissolution–precipitation reactions (e.g., Putnis 2009; Budzyń et al. 2021), and therefore also the extent of Pb-rich nanophase formation and retention of Pb*.

U–Pb systematics and monazite shock microstructures

Support for a Late Paleocene zircon U–Pb impact age for the Hiawatha impact structure

The monazite U–Pb data populate a discordant array, intercepting the concordia in the Paleoproterozoic (upper intercept) and the Late Paleocene (lower intercept; Fig. 11). Considering all monazite data from this study, despite having a high error, the lower intercept of 56 ± 27 Ma (MSWD = 15) is within an uncertainty of the 57.99 ± 0.54 Ma zircon U–Pb age for Hiawatha impact event that was obtained from the same samples (Figs. 1B, 11B; Kenny et al. 2022). Additionally, our data supports the Late Paleocene resetting of Ar–Ar dates of individual glassy sand-sized grains eroded from the crater (Kenny et al. 2022).

Although no concordant monazite ages (crystallisation) were recorded, as no undeformed grains were found, the upper intercept of 1911 ± 20 Ma from all monazite data likewise coincides with published U–Pb zircon ages from the Etah meta-igneous group and Etah meta-sedimentary successions which comprise the exposed foreland of the impact structure (Fig. 1B; Nutman et al. 2008; Dawes 2009) and dominate the target sequence of the impact structure (Garde et al. 2022; Hyde et al. 2023). Furthermore, this intercept age aligns with target rock ages form apparently unshocked zircon grains in the same samples (1905 ± 8 Ma; Kenny et al. 2022). Interestingly, no monazite analysis is located in an impact-induced Pb-loss discordia trending from the two other target rock ages that were identified from U–Pb zircon geochronology, ~ 1485 Ma and ~ 2300 Ma (Fig. 11A). These zircon age populations were interpreted to originate from the incorporation of other target rock lithologies or xenocrystic zircons within felsic intrusions. This indicates that all analysed monazite grains have a petrogenesis from the metamorphic event which formed the high-grade 1.95–1.75 Ga bedrock that dominates the exposed foreland in Inglefield Land (Fig. 1B; Nutman et al. 2008).

Shock and impact microstructures

The high spatial resolution of this SIMS study has made it possible to compare the shock microstructures and U–Pb apparent ages within individual parts of complex grains. Partially shock-recrystallised domains of two monazite grains show the most advanced U–Pb resetting (Fig. 11B; Table S1). The same microstructure–age resetting relationship, where recrystallised grains show the most advanced Pb loss, is observed in variably shocked monazites from other impact structures (e.g., Erickson et al. 2020) and in other U-bearing minerals, for example zircon (Kenny et al. 2019, 2022) and apatite (McGregor et al. 2018). Accordingly, analysis HW01-M23c which exclusively targeted a large neoblast, although removed from age determinations due to a Pb overcorrection, yielded an apparent age of 52.6 ± 3.1 Ma, younger than the adjacent analysis (HW01-M23b; 363 ± 16 Ma) situated in a largely non-neoblastic domain in the same grain (Figs. 5B, 11D; Table S1).

Analysis HW01-23a (154 ± 10 Ma) is located in an area containing both recrystallised and non-recrystallised monazite, as well as a set of impact-diagnostic $(10\bar{1})$ microtwins (Fig. 5B). This analysis gave an older apparent age than analysis *c*, but the second youngest age within the dataset (Table S1). Mechanical twinning in monazite, forming through simple shear of the crystal lattice in both tectonic- and impact-deformed monazite, has been shown to facilitate the expulsion of Pb* from the monazite lattice, leading to the partial to complete resetting of the U–Pb system (Erickson et al. 2017b; Fougerouse et al. 2020, 2021). Pb loss associated with twin formation in monazite was also demonstrated to be thermally dependant, requiring high temperatures (e.g., > 900 °C; Fougerouse et al. 2021). Indeed, grain 01-M23 was subjected to temperatures in excess of 900 °C from impact-generated melt injections seen here (Fig. 10). However, as the analysis (HW01-M23a) incorporated variably age reset material and the twin did not undergo recrystallisation (Fig. 10E), the preserved apparent age is not concordant (Fig. 11).

Grains with coexisting melt-bearing channels and crystal-plastic deformation show contrasting degrees of Pb loss and yielded vastly different apparent ages (Fig. 4; Table S1). This indicates variable U–Pb resetting between the grains and/or within each grain. Lattice strain in shock-deformed zircon and monazite has been shown to facilitate Pb loss (Moser et al. 2011; Cavosie et al. 2015; Erickson et al. 2017b). High dislocation densities in plastically deformed grains observed here (Fig. 8) may have provided fast diffusion pathways for Pb loss during shock, perhaps though pipe diffusion, as dislocations are suggested to have more significant diffusion characteristics in plastically deformed minerals (e.g., Verberne et al. 2022). Another consideration is the variable temperatures these grains experienced in the heterogeneous impact melt (Figs. 2, S1), which probably controlled the ability of melt-film injections or in situ melting in curvilinear fractures to occur.

Pore and Pb-rich nanophase formation and U–Pb systematics

The monazite grains displaying only porosity on various scales (Figs. 3, 7) analysed here all show some degree of Pb loss, albeit to a lower degree than recrystallised monazite grains (Fig. 11). The U–Pb data from porous monazite alone defines a discordant array between target rock ages and the zircon U–Pb impact age, yielding accurate, albeit relatively imprecise, intercept ages (Fig. 11; Kenny et al. 2022). Porous monazite can therefore be considered a viable material for impact geochronology. The absence of any shock effects (e.g., lattice strain, mechanical twins) in most grains suggests that the porosity is not pressure-dependant and that Pb* loss was not facilitated by fast diffusion pathways associated with such features, except, perhaps migration of Pb along former diffusion pathways or dislocations (Figs. 7, 8).

The Pb-rich nanophases and high-density element clusters in all non-recrystallised monazite domains (Fig. 9) indicates a high accumulation of Pb*, acting as Pb sinks (Seydoux-Guillaume et al. 2019; Turuani et al. 2023), which has resulted in incomplete age resetting and relatively old U–Pb apparent ages (Fig. 11C). As all data here plot conformably on a linear discordia that trends between monazite crystallisation and the robust ~ 58 Ma zircon U–Pb impact age from the same samples (Fig. 11; Kenny et al. 2022), the overriding cause for opening the U–Pb system in the monazite grains is impact-induced. This further suggests that Pb-rich nanophase formation occurred via impact-related heating and associated fluid interaction. Furthermore, the preservation of these nanoscale structures, alongside the partial Pb loss and discordance observed, precludes the notion that these grains are neoformed or crystallised as a result of the unmixing of coexisting SiO_2 and P-rich melts, as recently suggested for similar porous monazite in Libyan Desert Glass (Kovaleva et al. 2023). If true, grains here would have crystallised exclusive of pre-impact Pb* and should now yield concordant impact ages, which we do not observe (Fig. 11).

Previous work on Pb-rich nanophases in monazite showed that they can disturb U–Pb geochronology due to heterogeneous Pb* retention across grains, commonly leading to ambiguous, discordant geological apparent ages (Seydoux-Guillaume et al. 2003; Turuani et al. 2022). Interestingly, element clusters have been shown to have no impact on geochronology (Laurent et al. 2016; Seydoux-Guillaume et al. 2019; Turuani et al. 2022, 2023), whereas Turuani et al. (2022) shows that increased retention of radiogenic Pb-rich nanophases results in decreases in discordance. Due to the prevalence of both nanoscale features (Fig. 9), it is unlikely we will be able to isolate their independent effects on the geochronological data presented here, nor evaluate the role that temperature (e.g., Budzyń et al. 2021) or the physico-chemical characteristics of the monazite grains themselves (e.g., Grand'Homme et al. 2016) influenced coupled dissolution–precipitation reactions and the mobility of elements in monazite. However, we observe that domains of relatively high Th zonation have i) more nanopores and Pb-rich nanophases (Fig. 7E) and ii) contain higher Pb* concentrations and yield older apparent ages from U–Pb analyses (Figs. 6, S2; Table S1).

Interestingly, we find no relationship between the pervasiveness of porosity observed in BSE images (Fig. S2) and U–Pb apparent ages, with grains at either end of the discordant array looking largely microtexturally similar (Figs. 11C, S2). Further imaging and/or nanoscale chemical mapping (e.g., APT) of grains where no zoning is observed might be more appropriate to reveal a trend in porosity and apparent age here, where we suspect the abundance of Pb-rich nanophases will be a major control on any calculated age.

Conclusions

- We show that monazite from impact melt rocks from the Hiawatha impact structure exhibit various known features of shock metamorphism, including shock-specific microtwins and recrystallisation textures. Additionally, nanoscale characterisation of shock microstructures using TEM procedures reveals the non-recrystallised nature of shock-specific microtwins as well as the formation of individual cell structures and dislocations within plastically deformed grains.
- We find variably scaled porosity in all grains. Larger pores arranged in linear arrays likely formed along pre-existing, now annealed planer features (PFs), where Pb loss was initially facilitated via migration along diffusion pathways. However, pore formation in a random arrangement is more dependent on Th/REE-zoning and the length of exposure to high temperatures.
- Nanopores and spectacular radiogenic Pb-rich nanophases formed via dissolution–precipitation reactions during the impact-induced high-temperature excursion with the interaction of fluids. However, prerequisite element clusters (Ø < 15 nm) formed prior to the impact over extended time periods (since monazite crystallisation ca. ~ 1.9 Ga) through Th and U decay and associated lattice instabilities. The abundance of Pb-rich nanophases is due to both the initial physico-chemical characteristics (e.g., zoning) of the grains, as well as their exposure to high temperatures and fluids.
- Moreover, with the identification of cerussite and Pb_3O_4, we increase the number of known Pb-rich phases crystallising in monazite nanopores and support previous work suggesting the immediate availably of elements within the fluid determines the nucleating Pb-rich phase chemistry, e.g., CO or CO_2 contained within impact melt for cerussite crystallisation.
- Altogether, the monazite data yield a linear discordant population which has provided an accurate impact age for the Hiawatha impact structure of 56 ± 27 Ma (MSWD = 15), within error of the more precise 57.99 ± 0.54 Ma zircon U–Pb age from the same melt rock samples (Kenny et al. 2022).
- We further demonstrate that the integration of high-spatial microstructural characterisation and in situ high-resolution U–Pb analysis of shocked monazite allows for more effective dating of impact events, whereby U–Pb analyses targeted at recrystallised domains in monazite show the most advanced age resetting. However, no analysis was concordant, due to the analysis of mixed domains and the widespread retention of Pb* in the form of Pb-rich nanophases.
- While previous work has primarily targeted recrystallised monazite, we demonstrate by conducting a coupled EBSD, TEM and SIMS study employing state-of-the-art methods that porous monazite alone is a valuable impact microtexture, which has a good potential for U–Pb dating of impact events if recrystallised zircon is not available.

Supplementary Information The online version contains supplementary material available at https://doi.org/10.1007/s00410-024-02097-1.

Acknowledgements We thank Leif Johannson (Lund University) for help with the initial identification of shocked monazite within the samples, Kerstin Lindén for casting the epoxy mount containing the monazite grains, Heejin Jeon for assistance with U-Pb analyses and Liane Benning and Marcin Syczewski for assistance with EXCITE TNA funding. We also thank Anders Bjørk, Joseph A. MacGregor and Pierre Beck for sample collection and pay tribute to the memory of Jérémie Mouginot. The NordSIMS facility is supported by the Swedish Research Council and the Swedish Museum of Natural History; Swedish Research Council (Vetenskapsrådet) infrastructure grant no. 2017-00276 (M.J.W.). NordSIMS contribution number 758. This work was also supported by the Swedish Research Council (Vetenskapsrådet) starting grant no. 2020-04862 (G.G.K.), the Geocenter Denmark grant DALIA (Kurt H. Kjær) and the Independent Research Fund Denmark grant no. 0135-00163B (N.K.L.). This project has received funding from the European Union's Horizon 2020 research and innovation programme under grant agreement No 101005611 for Transnational Access conducted at Helmholtz-Zentrum Potsdam Deutsches GeoforschungsZentrum (GFZ) under access number EXCITE_TNA_C3_2023_03 (W.R.H). We thank the European Regional Development Fund and the State of Brandenburg for the Themis Z TEM (part of PISA). Finally, we would like to thank editor Daniela Rubatto and express our gratitude to A-M Seydoux-Guillaume and one anonymous reviewer for their constructive comments and revisions, which significantly improved the quality of this manuscript.

Funding Open access funding provided by Copenhagen University.

Data availability All data needed to evaluate the conclusions in the paper are present in the paper and/or the Supplementary Materials.

Open Access This article is licensed under a Creative Commons Attribution 4.0 International License, which permits use, sharing, adaptation, distribution and reproduction in any medium or format, as long as you give appropriate credit to the original author(s) and the source, provide a link to the Creative Commons licence, and indicate if changes were made. The images or other third party material in this article are included in the article's Creative Commons licence, unless indicated otherwise in a credit line to the material. If material is not included in the article's Creative Commons licence and your intended use is not permitted by statutory regulation or exceeds the permitted use, you will need to obtain permission directly from the copyright holder. To view a copy of this licence, visit http://creativecommons.org/licenses/by/4.0/.

References

Abramov O, Kring DA (2007) Numerical modeling of impact-induced hydrothermal activity at the Chicxulub crater. Meteorit Planet Sci 42:93–112. https://doi.org/10.1111/j.1945-5100.2007.tb00220.x

Aleinikoff JN, Schenck WS, Plank MO, Srogi LA, Fanning CM, Kamo SL, Bosbyshell H (2006) Deciphering igneous and metamorphic events in high-grade rocks of the Wilmington complex, Delaware: Morphology, cathodoluminescence and backscattered electron zoning, and SHRIMP U-Pb geochronology of zircon and monazite. Bull Geol Soc Am 118:39–64. https://doi.org/10.1130/B25659.1

Alwmark C, Bleeker W, Lecheminant A, Page L, Scherstén A (2017) An Early Ordovician 40 Ar-39 Ar age for the ~50 km Carswell impact structure, Canada. Geol Soc Am Bull 11:1442–1449. https://doi.org/10.1130/B31666.1

Barralet J, Knowles JC, Best S, Bonfield W (2002) Thermal decomposition of synthesised carbonate hydroxyapatite. J Mater Sci Mater Med 13:529–533. https://doi.org/10.1023/A:1015175108668

Boher P, Garnier P, Gavarri JR, Hewat AW (1985) Monoxyde quadratique PbOα(I): Description de la transition structurale ferroe ´lastique. J Solid State Chem 57:343–350. https://doi.org/10.1016/0022-4596(85)90197-5

Bohor BF, Betterton WJ, Krogh TE (1993) Impact-shocked zircons: discovery of shock-induced textures reflecting increasing degrees of shock metamorphism. Earth Planet Sci Lett 119:419–424. https://doi.org/10.1016/0012-821X(93)90149-4

Bolzan AA, Fong C, Kennedy BJ, Howard CJ (1997) Structural studies of rutile-type metal dioxides. Acta Crystallogr B 53:373–380. https://doi.org/10.1107/S0108768197001468

Bouad N, Chapon L, Marin-Ayral RM, Bouree-Vigneron F, Tedenac JC (2003) Neutron powder diffraction study of strain and crystallite size in mechanically alloyed PbTe. J Solid State Chem 173:189–195. https://doi.org/10.1016/S0022-4596(03)00017-3

Bouvaist J, Weigel D (1970) Sesquioxyde de plomb, Pb2O3. I. Determination DE La Structure. Acta Crystallogr Sect A 26:501–510. https://doi.org/10.1107/S0567739470001316

Budzyń B, Wirth R, Sláma J, Birski Ł, Tramm F, Kozub-Budzyń GA, Rzepa G, Schreiber A (2021) LA-ICPMS, TEM and Raman study of radiation damage, fluid-induced alteration and disturbance of U-Pb and Th-Pb ages in experimentally metasomatised monazite. Chem Geol. https://doi.org/10.1016/j.chemgeo.2021.120464

Budzyń B, Wirth R, Sláma J, Kozub-Budzyń GA, Rzepa G, Schreiber A (2022) A detailed and comprehensive TEM, EPMA and Raman characterization of high-metamorphic grade monazites and their U-Th-Pb systematics (the Góry Sowie Block, SW Poland). Chem Geol. https://doi.org/10.1016/j.chemgeo.2022.121015

Cavosie AJ, Erickson TM, Timms NE, Reddy SM, Talavera C, Montalvo SD, Pincus MR, Gibbon RJ, Moser D (2015) A terrestrial perspective on using ex situ shocked zircons to date lunar impacts. Geology 43:999–1002. https://doi.org/10.1130/G37059.1

Cavosie AJ, Timms NE, Erickson TM, Hagerty JJ, Hörz F (2016) Transformations to granular zircon revealed: twinning, reidite, and ZrO2 in shocked zircon from Meteor Crater (Arizona, USA). Geology 44:703–706. https://doi.org/10.1130/G38043.1

Cavosie AJ, Kirkland CL, Reddy SM, Timms NE, Talavera C, Pincus MR (2021) Extreme plastic deformation and subsequent Pb loss in shocked xenotime from the Vredefort Dome, South Africa (W. U. Reimold & C. Koeberl, Eds.): Large Meteorite Impacts and Planetary Evolution VI, 550, p. 0, https://doi.org/10.1130/2021.2550(20).

Cox MA, Erickson TM, Schmieder M, Christoffersen R, Ross DK, Cavosie AJ, Bland PA, Kring DA (2020) High-resolution microstructural and compositional analyses of shock deformed apatite from the peak ring of the Chicxulub Impact Crater. Meteorit Planet Sci 1733:1715–1733. https://doi.org/10.1111/maps.13541

Davis DW (2008) Sub-million-year age resolution of Precambrian igneous events by thermal extraction-thermal ionization mass spectrometer Pb dating of zircon: Application to crystallization of the Sudbury impact melt sheet. Geology 36:383–386. https://doi.org/10.1130/G24502A.1

Dawes PR (2009) Precambrian-Palaeozoic geology of Smith Sound, Canada and Greenland: Key constraint to palaeogeographic reconstructions of northern Laurentia and the North Atlantic region. Terra Nova 21:1–13. https://doi.org/10.1111/j.1365-3121.2008.00845.x

Erickson TM, Pearce MA, Taylor RJM, Timms NE, Clark C, Reddy SM, Buick IS (2015) Deformed monazite yields high-temperature tectonic ages. Geology 43:383–386. https://doi.org/10.1130/G36533.1

Erickson TM, Cavosie AJ, Pearce MA, Timms NE, Reddy SM (2016) Empirical constraints on shock features in monazite using shocked zircon inclusions. Geology 44:635–638. https://doi.org/10.1130/G37979.1

Erickson TM, Pearce MA, Reddy SM, Timms NE, Cavosie AJ, Bourdet J, Rickard WDA, Nemchin AA (2017a) Microstructural constraints on the mechanisms of the transformation to reidite in naturally shocked zircon. Contrib Mineral Petrol. https://doi.org/10.1007/s00410-016-1322-0

Erickson TM, Timms NE, Kirkland CL, Tohver E, Cavosie AJ, Pearce MA, Reddy SM (2017b) Shocked monazite chronometry: integrating microstructural and in situ isotopic age data for determining precise impact ages. Contrib Miner Petrol 172:1–19. https://doi.org/10.1007/s00410-017-1328-2

Erickson TM, Timms NE, Pearce MA, Cayron C, Deutsch A, Keller LP, Kring DA (2019) Shock-produced high-pressure (La, Ce, Th)PO4 polymorph revealed by microstructural phase heritage of monazite. Geology 47:504–508. https://doi.org/10.1130/G46008.1

Erickson TM, Kirkland CL, Timms NE, Cavosie AJ, Davison TM (2020) Precise radiometric age establishes Yarrabubba, Western Australia, as Earth's oldest recognised meteorite impact structure. Nat Commun 11:1–8. https://doi.org/10.1038/s41467-019-13985-7

Erickson TM, Kirkland CL, Jourdan F, Schmieder M, Hartnady MIH, Cox MA, Timms NE (2021) Resolving the age of the Haughton impact structure using coupled 40Ar/39Ar and U-Pb geochronology. Geochim Cosmochim Acta 304:68–82. https://doi.org/10.1016/j.gca.2021.04.008

Flowers RM, Moser DE, Hart RJ (2003) Evolution of the amphibolite-granulite facies transition exposed by the Vredefort impact structure Kaapvaal Craton, South Africa. J Geol 111:455–470. https://doi.org/10.1086/375282

Fougerouse D, Reddy SM, Seydoux-Guillaume AM, Kirkland CL, Erickson TM, Saxey DW, Rickard WDA, Jacob D, Leroux H, Clark C (2020) Mechanical twinning of monazite expels radiogenic lead. Geology 49:417–421. https://doi.org/10.1130/G48400.1

Fougerouse D, Cavosie AJ, Erickson T, Reddy SM, Cox MA, Saxey DW, Rickard WDA, Wingate MTD (2021) A new method for dating impact events—thermal dependency on nanoscale Pb mobility in monazite shock twins. Geochim Cosmochim Acta 314:381–396. https://doi.org/10.1016/j.gca.2021.08.025

French BM, Koeberl C (2010) The convincing identification of terrestrial meteorite impact structures: What works, what doesn't, and why. Earth-Sci Rev 98:123–170. https://doi.org/10.1016/j.earscirev.2009.10.009

Garde AA, Keulen N, Waight T (2022) Microporphyritic and microspherulitic melt grains, Hiawatha crater, Northwest Greenland: Implications for post-impact cooling rates, hydration, and the cratering environment. GSA Bull 134:2145–2166. https://doi.org/10.1130/B36058.1/5504875/b36058.pdf

Garneir P, Moreua J, Gavarri JR (1990) Analyse de rietveld de la structure de Pb1−xTixO1+x par diffraction des neutrons. Mater Res Bull 25:979–986

Gavarri JR, Weigel D (1975) Oxydes de plomb. I. Structure cristalline du minium Pb3O4, à température ambiante (293 K). J Solid State Chem 13:252–257. https://doi.org/10.1016/0022-4596(75)90127-9

Geisler T, Schaltegger U, Tomaschek F (2007) Re-equilibration of zircon in aqueous fluids and melts. Elements 3:43–50. https://doi.org/10.2113/gselements.3.1.43

Goltrant O, Leroux H, Doukhan JC, Cordier P (1992) Formation mechanisms of planar deformation features in naturally shocked quartz. Phys Earth Planet Inter 74:219–240. https://doi.org/10.1016/0031-9201(92)90012-K

Grand'Homme A, Janots E, Seydoux-Guillaume AM, Guillaume D, Bosse V, Magnin V (2016) Partial resetting of the U-Th-Pb systems in experimentally altered monazite: Nanoscale evidence of incomplete replacement. Geology 44:431–434. https://doi.org/10.1130/G37770.1

Grand'Homme A, Janots E, Seydoux-Guillaume AM, Guillaume D, Magnin V, Hövelmann J, Höschen C, Boiron MC (2018) Mass transport and fractionation during monazite alteration by anisotropic replacement. Chem Geol 484:51–68. https://doi.org/10.1016/j.chemgeo.2017.10.008

Grocholski B, Shim SH, Cottrell E, Prakapenka VB (2014) Crystal structure and compressibility of lead dioxide up to 140 GPa. Am Mineralog 99:170–177. https://doi.org/10.2138/am.2014.4596

Hart R, Moser D, Andreoli M (1999) Archean age for the granulite facies metamorphism near the center of the Vredefort structure, South Africa. Geology 27:1091–1094. https://doi.org/10.1130/0091-7613(1999)027%3c1091:AAFTGF%3e2.3.CO;2

Hay DC, Dempster TJ (2009) Zircon behaviour during low-temperature metamorphism. J Petrol 50:571–589. https://doi.org/10.1093/petrology/egp011

Hay RS, Marshall DB (2003) Deformation twinning in Monazite. Acta Material 51:5235–5254. https://doi.org/10.1016/S1359-6454(03)00305-7

Hyde WR, Garde AA, Keulen N, Malkki SN, Jaret SJ, McDonald I, Beck P, Larsen NK (2023) Impact melt rocks from the Late Paleocene Hiawatha impact structure, northwest Greenland. Meteor Planet Sci 58:789–814. https://doi.org/10.1111/maps.13987

Jourdan F, Reimold WU, Deutsch A (2012) Dating terrestrial impact structures. Elements 8:49–53. https://doi.org/10.2113/gselements.8.1.49

Kenny GG, Schmieder M, Whitehouse MJ, Nemchin AA, Morales LFG, Buchner E, Bellucci JJ, Snape JF (2019) A new U-Pb age for shock-recrystallised zircon from the Lappajärvi impact crater, Finland, and implications for the accurate dating of impact events. Geochim Cosmochim Acta 245:479–494. https://doi.org/10.1016/j.gca.2018.11.021

Kenny GG, Karlsson A, Schmieder M, Whitehouse MJ, Nemchin AA, Bellucci JJ (2020) Recrystallization and chemical changes in apatite in response to hypervelocity impact. Geology 48:19–23. https://doi.org/10.1130/G46575.1

Kenny GG, Harrigan CO, Schmitz MD, Crowley JL, Wall CJ, Andreoli MAG, Gibson RL, Maier WD (2021) Timescales of impact melt sheet crystallization and the precise age of the Morokweng impact structure, South Africa. Earth Planet Sci Lett 567:117013. https://doi.org/10.1016/j.epsl.2021.117013

Kenny GG et al (2022) A Late Paleocene age for Greenland's Hiawatha impact structure. Sci Adv. https://doi.org/10.1126/sciadv.abm2434

Kirkland CL, Whitehouse MJ, Slagstad T (2009) Fluid-assisted zircon and monazite growth within a shear zone: A case study from Finnmark, Arctic Norway. Contrib Mineral Petrol 158:637–657. https://doi.org/10.1007/s00410-009-0401-x

Kjær KH et al (2018) A large impact crater beneath Hiawatha Glacier in northwest Greenland. Sci Adv 4:1–11. https://doi.org/10.1126/sciadv.aar8173

Kovaleva E, Dixon R (2020) Properties of impact-related Pseudotachylite and associated shocked zircon and monazite in the upper levels of a large impact basin: a case study from the Vredefort impact structure. Minerals 10:1–22. https://doi.org/10.3390/min10121053

Kovaleva E, Helmy H, Belkacim S, Schreiber A, Wilke FDH, Wirth R (2023) Libyan Desert Glass: new evidence for an extremely high-pressure-temperature impact event from nanostructural study. Am Miner 108:1906–1923. https://doi.org/10.2138/am-2022-8759

Krogh TE, Davis DW, Corfu F (1984) Precise U-Pb zircon and baddeleyite ages for the sudbury area: In: Pye EG, Naldrett AJ, Giblin PE (eds) The Geology and ore deposits of the sudbury structure ontario geological survey, specifications, 1, p. 431–446

Kusiak MA, Dunkley DJ, Wirth R, Whitehouse MJ, Wilde SA, Marquardt K (2015) Metallic lead nanospheres discovered in ancient zircons. Proc Natl Acad Sci USA 112:4958–4963. https://doi.org/10.1073/pnas.1415264112

Kusiak MA, Kovaleva E, Vanderliek D, Becker H, Wilke F, Schreiber A, Wirth R (2022) Nano- and micro-structures in lunar zircon from Apollo 15 and 16 impactites: implications for age interpretations. Contrib Miner Petrol 177:1–20. https://doi.org/10.1007/s00410-022-01977-8

Laurent AT, Seydoux-Guillaume AM, Duchene S, Bingen B, Bosse V, Datas L (2016) Sulphate incorporation in monazite lattice and dating the cycle of sulphur in metamorphic belts. Contrib Miner Petrol 171:1–19. https://doi.org/10.1007/s00410-016-1301-5

Leroux H, Reimold WU, Koeberl C, Hornemann U, Doukhan JC (1999) Experimental shock deformation in zircon: a transmission electron microscopic study. Earth Planet Sci Lett 169:291–301. https://doi.org/10.1016/S0012-821X(99)00082-5

Lindgren P, Hallis L, Hage FS, Lee MR, Parnell J, Plan A, Doye A, MacLaren I (2019) A TEM and EELS study of carbon in a melt fragment from the Gardnos impact structure. Meteor Planet Sci 54:2698–2709. https://doi.org/10.1111/maps.13381

Ludwig KR (1998) On the treatment of concordant uranium-lead ages. Geochim Cosmochim Acta 62:665–676. https://doi.org/10.1016/S0016-7037(98)00059-3

Martell J, Alwmark C, Holm-Alwmark S, Lindgren P (2021) Shock deformation in zircon grains from the Mien impact structure, Sweden. Meteor Planet Sci 56:362–378. https://doi.org/10.1111/maps.13625

McGregor M, McFarlane CRM, Spray JG (2018) In situ LA-ICP-MS apatite and zircon U-Pb geochronology of the Nicholson Lake impact structure, Canada: shock and related thermal effects. Earth Planet Sci Lett 504:185–197. https://doi.org/10.1016/j.epsl.2018.10.006

McGregor M, McFarlane CRM, Spray JG (2019) In situ multiphase U-Pb geochronology and shock analysis of apatite, titanite and zircon from the Lac La Moinerie impact structure, Canada. Contrib Mineral Petrol. https://doi.org/10.1007/s00410-019-1598-y

McGregor M, Dence MR, McFarlane CRM, Spray JG (2020) U-Pb geochronology of apatite and zircon from the Brent impact structure, Canada: a Late Ordovician Sandbian-Katian boundary event associated with L-Chondrite parent body disruption. Contrib Mineral Petrol 175:1–21. https://doi.org/10.1007/s00410-020-01699-9

McGregor M, Erickson TM, Spray JG, Whitehouse MJ (2021) High-resolution EBSD and SIMS U-Pb geochronology of zircon, titanite, and apatite: insights from the Lac La Moinerie impact structure, Canada. Contrib Mineral Petrol 176:1–25. https://doi.org/10.1007/s00410-021-01828-y

Minch R, Peters L, Ehm L, Knorr K, Siidra OI, Prakapenka V, Dera P, Depmeier W (2010) Evidence for the existence of a PbCO3-II phase from high pressure X-ray measurements. Zeitschrift Fur Kristallographie 225:146–152. https://doi.org/10.1524/zkri.2010.1194

Moser DE (1997) Dating the shock wave and thermal imprint of the giant Vredefort impact, South Africa. Geology 25:7–10. https://doi.org/10.1130/0091-7613(1997)025%3c0007:DTSWAT%3e2.3.CO;2

Moser DE, Cupelli CL, Barker IR, Flowers RM, Bowman JR, Wooden J, Hart JR (2011) New zircon shock phenomena and their use for dating and reconstruction of large impact structures revealed by electron nanobeam (EBSD, CL, EDS) and isotopic U-Pb and (U-Th)/he analysis of the vredefort dome. Can J Earth Sci 48:117–139. https://doi.org/10.1139/E11-011

Ni Y, Hughes JM, Mariano AN, Et NI, Crystal AL (1995) Crystal chemistry of the monazite and xenotime structures tetrahedra and RE polyhedra, with a REOg polyhedron in xenotime that accommodates the heavy lanthanides (Tb-Lu in the synthetic phases) and a RE09 polyhedron in monazite that preferentially inco. Am Mineral 80:21–26

Nutman AP, Dawes PR, Kalsbeek F, Hamilton MA (2008) Palaeoproterozoic and Archaean gneiss complexes in northern Greenland: Palaeoproterozoic terrane assembly in the High Arctic. Precambr Res 161:419–451. https://doi.org/10.1016/j.precamres.2007.09.006

Osinski GR et al (2022) Impact Earth: A review of the terrestrial impact record. Earth Sci Rev. https://doi.org/10.1016/j.earscirev.2022.104112

Papapavlou K, Darling JR, Moser DE, Barker IR, White LF, Lightfoot PC, Storey CD, Dunlop J (2018) U-Pb isotopic dating of titanite microstructures: potential implications for the chronology and identification of large impact structures. Contrib Miner Petrol 173:1–15. https://doi.org/10.1007/s00410-018-1511-0

Plan A, Kenny GG, Erickson TM, Lindgren P, Alwmark C, Holm-Alwmark S, Lambert P, Scherstén A, Söderlund U (2021) Exceptional preservation of reidite in the Rochechouart impact structure, France: new insights into shock deformation and phase transition of zircon. Meteor Planet Sci 56:1795–1828. https://doi.org/10.1111/maps.13723

Putnis A (2009) Mineral replacement reactions. Rev Mineral Geochem 70:87–124. https://doi.org/10.2138/rmg.2009.70.3

Schärer U, Deutsch A (1990) Isotope systematics and shock-wave metamorphism: II. U-Pb and Rb-Sr in naturally shocked rocks; the Haughton Impact Structure, Canada. Geochim Cosmochim Acta 54:3435–3447. https://doi.org/10.1016/0016-7037(90)90296-W

Schmieder M, Jourdan F (2013) The Lappajärvi impact structure (Finland): age, duration of crater cooling, and implications for early life. Geochim Cosmochim Acta 112:321–339. https://doi.org/10.1016/j.gca.2013.02.015

Schmieder M, Kring DA (2020) Earth's impact events through geologic time: a list of recommended ages for terrestrial impact structures and deposits. Astrobiology 20:91–141. https://doi.org/10.1089/ast.2019.2085

Seydoux-Guillaume AM, Paquette JL, Wiedenbeck M, Montel JM, Heinrich W (2002) Experimental resetting of the U-Th-Pb systems in monazite. Chem Geol 191:165–181. https://doi.org/10.1016/S0009-2541(02)00155-9

Seydoux-Guillaume AM, Goncalves P, Wirth R, Deutsch A (2003) Transmission electron microscope study of polyphase and discordant monazites: site-specific specimen preparation using the focused ion beam technique. Geology 31:973–976. https://doi.org/10.1130/G19582.1

Seydoux-Guillaume AM, Wirth R, Deutsch A, Schärer U (2004) Microstructure of 24–1928 Ma concordant monazites; implications for geochronology and nuclear waste deposits. Geochim Cosmochim Acta 68:2517–2527. https://doi.org/10.1016/j.gca.2003.10.042

Seydoux-Guillaume A-M, Deschanes X, Baumier C, Neumeier S, Weber WJ, Peuget S (2018b) Why natural monazite never becomes amorphous: experimental evidence for alpha self-healing. Am Miner 103:824–827

Seydoux-Guillaume AM, Fougerouse D, Laurent AT, Gardés E, Reddy SM, Saxey DW (2019) Nanoscale resetting of the Th/Pb system in an isotopically-closed monazite grain: a combined atom probe and transmission electron microscopy study. Geosci Front 10:65–76. https://doi.org/10.1016/j.gsf.2018.09.004

Seydoux-Guillaume AM, de Resseguier T, Montagnac G, Reynaud S, Leroux H, Reynard B, Cavosie AJ (2022) Bridging the shocked monazite gap—deformation microstructures in natural and laser shock-loaded samples. Earth Planet Sci Lett 595:117727. https://doi.org/10.1016/j.epsl.2022.117727

Seydoux-Guillaume A-M, Bingen B, Bosse V, Janots E, Laurent AT (2018a) Transmission electron microscope imaging sharpens geochronological interpretation of zircon and monazite. In: Microstructural geochronology: planetary records down to atom scale. American Geophysical Union, pp 261–275

Silva D, Lana C, de Souza Filho CR (2016) Petrographic and geochemical characterization of the granitic rocks of the Araguainha impact crater, Brazil. Meteor Planet Sci 51:443–467. https://doi.org/10.1111/maps.12601

Stacey JS, Kramers JD (1975) Approximation of terrestrial lead isotope evolution by a two-stage model. Earth Planet Sci Lett 26:207–221. https://doi.org/10.1016/0012-821X(75)90088-6

Steiger R, Jäger E (1997) Subcommission on geochronology: convention on the use of decay constants in geo- and cosmochronology. Earth Planet Sci Lett 35:359–362. https://doi.org/10.3109/00016488809106418

Timms NE, Erickson TM, Pearce MA, Cavosie AJ, Schmieder M, Tohver E, Reddy SM, Zanetti MR, Nemchin AA, Wittmann A (2017) A pressure-temperature phase diagram for zircon at extreme conditions. Earth Sci Rev 165:185–202. https://doi.org/10.1016/j.earscirev.2016.12.008

Tohver E et al (2012) Geochronological constraints on the age of a Permo-Triassic impact event: U-Pb and 40Ar/ 39Ar results for the 40km Araguainha structure of central Brazil. Geochim Cosmochim Acta 86:214–227. https://doi.org/10.1016/j.gca.2012.03.005

Turuani MJ, Laurent AT, Seydoux-Guillaume AM, Fougerouse D, Saxey D, Reddy SM, Harley SL, Reynaud S, Rickard WDA (2022) Partial retention of radiogenic Pb in galena nanocrystals explains discordance in monazite from Napier Complex (Antarctica). Earth Planet Sci Lett 588:117567. https://doi.org/10.1016/j.epsl.2022.117567

Turuani MJ et al (2023) Nanoscale features revealed by a multiscale characterization of discordant monazite highlight mobility mechanisms of Th and Pb. Contrib Mineral Petrol. https://doi.org/10.1007/s00410-023-02015-x

Verberne R, Reddy SM, Saxey DW, Fougerouse D, Rickard WDA, Quadir Z, Evans NJ, Clark C (2022) Dislocations in minerals: fast-diffusion pathways or trace-element traps? Earth Planet Sci Lett 584:117517. https://doi.org/10.1016/j.epsl.2022.117517

Vermeesch P (2018) IsoplotR: A free and open toolbox for geochronology. Geosci Front 9:1479–1493. https://doi.org/10.1016/j.gsf.2018.04.001

Wirth R (2004) Focused Ion Beam (FIB): A novel technology for advanced application of micro- and nanoanalysis in geosciences and applied mineralogy. Eur J Mineral 16:863–876. https://doi.org/10.1127/0935-1221/2004/0016-0863

Wirth R (2009) Focused Ion Beam (FIB) combined with SEM and TEM: Advanced analytical tools for studies of chemical composition, microstructure and crystal structure in geomaterials on a nanometre scale. Chem Geol 261:217–229. https://doi.org/10.1016/j.chemgeo.2008.05.019

Wittmann A, Kenkmann T, Schmitt RT, Stöffler D (2006) Shock-metamorphosed zircon in terrestrial impact craters. Meteorit Planet Sci 41:433–454. https://doi.org/10.1111/j.1945-5100.2006.tb00472.x

Wittmann A, Goderis S, Claeys P, Vanhaecke F, Deutsch A, Adolph L (2013) Petrology of impactites from El'gygytgyn crater: Breccias in ICDP-drill core 1C, glassy impact melt rocks and spherules. Meteor Planet Sci 48:1199–1235. https://doi.org/10.1111/maps.12019

Zeuthen CM, Thorup PS, Roth N, Iversen BB (2020) Reconciling crystallographic and physical property measurements on thermoelectric lead sulfide. J Am Chem Soc 141:8146–8157. https://doi.org/10.1021/jacs.9b00043

Zhang AC, Hsu WB, Li XH, Ming HL, Li QL, Liu Y, Tang GQ (2011) Impact melting of lunar meteorite Dhofar 458: evidence from polycrystalline texture and decomposition of zircon. Meteor Planet Sci 46:103–115. https://doi.org/10.1111/j.1945-5100.2010.01144.x

Publisher's Note Springer Nature remains neutral with regard to jurisdictional claims in published maps and institutional affiliations.